Please cite this article as: Susaki and Ueda, Whole-body and Whole-Organ Clearing and Imaging Techniques with Single-Cell Resolution: Toward Organism-Level Systems Biology in Mammals, Cell Chemical Biology (2016), http://dx.doi.org/10.1016/j.chembiol.2015.11.009

Cell Chemical Biology
Review

Whole-body and Whole-Organ Clearing and Imaging Techniques with Single-Cell Resolution: Toward Organism-Level Systems Biology in Mammals

Etsuo A. Susaki[1,2,3,4] and Hiroki R. Ueda[1,3,4,*]
[1]Department of Systems Pharmacology, Graduate School of Medicine, The University of Tokyo, 7-3-1 Hongo, Bunkyo-ku, Tokyo 113-0033, Japan
[2]PRESTO, Japan Science and Technology Agency (JST), 4-1-8 Honcho, Kawaguchi, Saitama, 332-0012, Japan
[3]Laboratory for Synthetic Biology, RIKEN Quantitative Biology Center (QBiC), 1-3, Yamadaoka, Suita, Osaka 565-0874, Japan
[4]AMED-CREST, Japan Agency for Medical Research and Development (AMED), 1-7-1, Ohte-machi, Chiyoda-ku, Tokyo, 100-0004, Japan
*Correspondence: uedah-tky@umin.ac.jp
http://dx.doi.org/10.1016/j.chembiol.2015.11.009

Organism-level systems biology aims to identify, analyze, control and design cellular circuits in organisms. Many experimental and computational approaches have been developed over the years to allow us to conduct these studies. Some of the most powerful methods are based on using optical imaging in combination with fluorescent labeling, and for those one of the long-standing stumbling blocks has been tissue opacity. Recently, the solutions to this problem have started to emerge based on whole-body and whole-organ clearing techniques that employ innovative tissue-clearing chemistry. Here, we review these advancements and discuss how combining new clearing techniques with high-performing fluorescent proteins or small molecule tags, rapid volume imaging and efficient image informatics is resulting in comprehensive and quantitative organ-wide, single-cell resolution experimental data. These technologies are starting to yield information on connectivity and dynamics in cellular circuits at unprecedented resolution, and bring us closer to system-level understanding of physiology and diseases of complex mammalian systems.

Introduction

The life sciences have been experiencing a revolutionary period since around the turn of Twenty-first century, when the massive efforts to determine the genomic sequences of various model organisms began to yield fruit. At that time, a fledgling discipline of systems biology began to emerge as an extension of the traditional molecular biology and was fueled by the large volumes of data and systems level views of cells and organism coming out of genome sequencing efforts. Further advancements in "omics" methods beyond genomics, such as proteomics, transcriptomics, lipidomics, metabolomics, and similar, emerged and further expanded the scope and reach of systems biology in the post genome era. Early on, systems biology introduced a number of interesting concepts and systems-biological approaches to be applied to fundamental questions mainly within the molecular-to-cellular layer, which over time developed into four interacting research domains: (1) identification of components of the system, (2) analysis of the system, (3) control of the system, and (4) reconstitution and design of the system (Kitano, 2002). Although the development of various technologies in the molecular-to-cellular level of analysis has been prosperous, systems-biological approaches in the upper-layer of multicellular organisms, the cellular-to-organ layer, has been limited until recently.

Considering that the structure and function of an organism are an ultimate manifestation of a collective output from all cellular circuits within that organism, there is an obvious need to develop technologies that would allow us to comprehensively identify and quantitatively analyze cellular circuits within an organism in order to better understand its anatomy and physiology. In particular, the realization of systems biology in the cellular-to-organism layer ("organism-level systems biology") is of special importance in mammalian research because of its wide range of applicability to life and health sciences. From this point of view, the recent developments of whole-body and whole-organ clearing and imaging technologies with single-cell resolution are opening the door toward organism-level systems biology. These technologies have started to provide comprehensive and quantitative experimental data in the cell-to-organism layer. In this review, we propose a plausible roadmap for realizing the organism-level systems biology in mammals by reviewing the recent methodological achievements in whole-body and whole-organ clearing and imaging, as well as cellular labeling and image informatics (Figure 1). These technologies constitute the versatile experimental platform for this rapidly developing research field, which will support further acceleration of life and health sciences.

Chemical Approach of Tissue Clearing for Whole-Body and Whole-Organ Imaging

Optical imaging, particularly in combination with fluorescent labeling of cells, is one of the practical ways for collecting single-cell resolution information inside an organ or a body because of its good spatial resolution and high signal-to-noise ratio. Tissue opacity, however, is one of the major obstacles in whole-body and whole-organ optical imaging. Tissues consist of various substances with different optical properties (Tuchin, 2015). Therefore, when the light goes through tissues, light distribution and intensity become broadened and decayed due to light scattering and light absorption, respectively, which causes

Please cite this article as: Susaki and Ueda, Whole-body and Whole-Organ Clearing and Imaging Techniques with Single-Cell Resolution: Toward Organism-Level Systems Biology in Mammals, Cell Chemical Biology (2016), http://dx.doi.org/10.1016/j.chembiol.2015.11.009

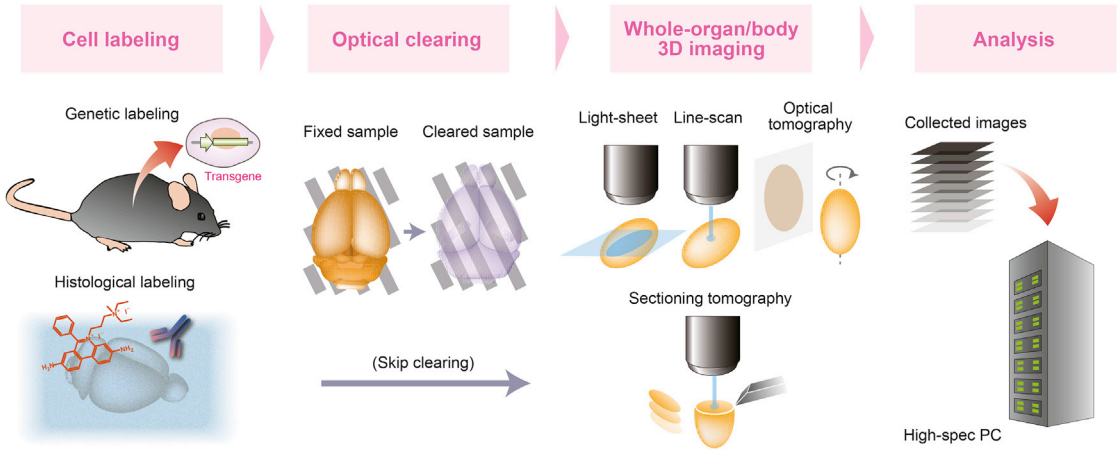

Figure 1. Steps for Organism-Level Systems Biology
Overview of the proposed research scheme, aiming at organism-level systems biology in mammal by comprehensive cell detection and analysis of whole-organ/body. This is achieved by optical tissue clearing and imaging (or alternatively by sectioning tomography without clearing) of properly labeled specimens. Data are analyzed to extract biological information, for which high-spec PC equipment is generally needed.

blurred and weakened images, especially in deeper regions of the tissue. Thus, the purpose of tissue clearing is mainly to minimize light scattering and absorption for better optical imaging. Efficient tissue clearing contributes to improved imaging depth and contrast (Cicchi et al., 2005; Vargas et al., 2001), which is necessary to support progress in whole-body and whole-organ 3D imaging. Although tissue clearing has a history that's more than 100 years long (Spalteholz, 1914; Zhu et al., 2013), tissue-clearing methods that can be implemented on practical timescales of days to weeks with a reasonable clearing efficiency for optic imaging are a much more recent development (Hama et al., 2015; Miyawaki, 2015; Ode and Ueda, 2015; Richardson and Lichtman, 2015). In this section, we will first discuss light scattering and light absorption, two physical properties of biological specimens that make whole-organ and whole-body clearing necessary, highlight basic principles of currently available methods of tissue clearing, and discuss some of the outstanding obstacles to whole-body and whole-organ imaging.

Physical Properties of Biological Specimens that Interfere with Whole-Body and Whole-Organ Imaging

One important obstacle for the light transmittance is light scattering. A biological specimen consists of various substances of different optical properties. In the tissue, biological substances such as water, lipids, proteins, and minerals usually exist as an inhomogeneous mixture (Figures 2A and 2B). Their inhomogeneous distributions cause strong lateral scattering and thus light cannot pass straight through a tissue for the forward direction (Richardson and Lichtman, 2015; Tuchin, 2015) (Figure 2A). Furthermore, biological substances sometimes form inhomogeneous structures inside and outside cells, which also causes light scattering and are another reason for tissue opacity (Johnsen and Widder, 1999; Tuchin, 2015) (Figures 2A and 2B). These include lipid particles and organelles (e.g., mitochondria), large protein clusters (e.g., collagen fibers), or even whole cell volume (e.g., red blood cells) (Beauvoit et al., 1994; Beuthan et al., 1996; Mourant et al., 1998; Steinke and Shepherd, 1988; van Staveren et al., 1991; Wen et al., 2009; Yeh and Hirshburg, 2006). These particles cause either the so-called Rayleigh scattering (the reason that the sky is blue) or Mie scattering (the reason that milk is white), depending on their sizes. Therefore, this point is important in considering the various clearing efficiencies of different organs (Susaki et al., 2015; Tainaka et al., 2014) or different regions within the same organ (e.g., gray matter and white matter in the brain) (Ke et al., 2013; Susaki et al., 2014), because the degree of light scattering is different among different organs and regions inside an organ (Cheong et al., 1990), probably due to the difference in their components and microscopic structures. Furthermore, fixation may affect the clearing efficiency because of differing features or density of the cross-link reaction. We found out that the pH of paraformaldehyde is a critical factor for the subsequent clearing step with the CUBIC (clear, unobstructed brain/body imaging cocktails and computational analysis) protocol, probably attributable to the difference in pH-dependent fixation efficiency (Susaki et al., 2015).

Another important obstacle for the light transmittance is light absorption by biological substances (Figures 2A and 2C). Light absorption is the transformation of light energy to some other form of energy (e.g., heat), which causes decay of light intensity during its travel within a tissue (Tuchin, 2015). Intrinsic light-absorbing substances in tissue, particularly heme and melanin pigments, have high light-absorption ability within the visible light range (400–600 nm) (Horecker, 1943; Tuchin, 2015; Weissleder, 2001). The removal of these internal light absorbers therefore contributes to translucency of animals, which was evidenced by translucent fish models of pigmentation mutants (Wakamatsu et al., 2001; White et al., 2008). Considering all of these reasons, strategies for tissue clearing are therefore aimed at minimization of light scattering and light absorption inside the tissue (Figure 2A).

Minimization of Light Scattering by RI Matching

As discussed above, light scattering inside a tissue is one of the main reasons of tissue opacity. Tissue clearing thus can be achieved by homogenization of optical property inside the tissue

 ©2016 Elsevier Ltd All rights reserved

Please cite this article as: Susaki and Ueda, Whole-body and Whole-Organ Clearing and Imaging Techniques with Single-Cell Resolution: Toward Organism-Level Systems Biology in Mammals, Cell Chemical Biology (2016), http://dx.doi.org/10.1016/j.chembiol.2015.11.009

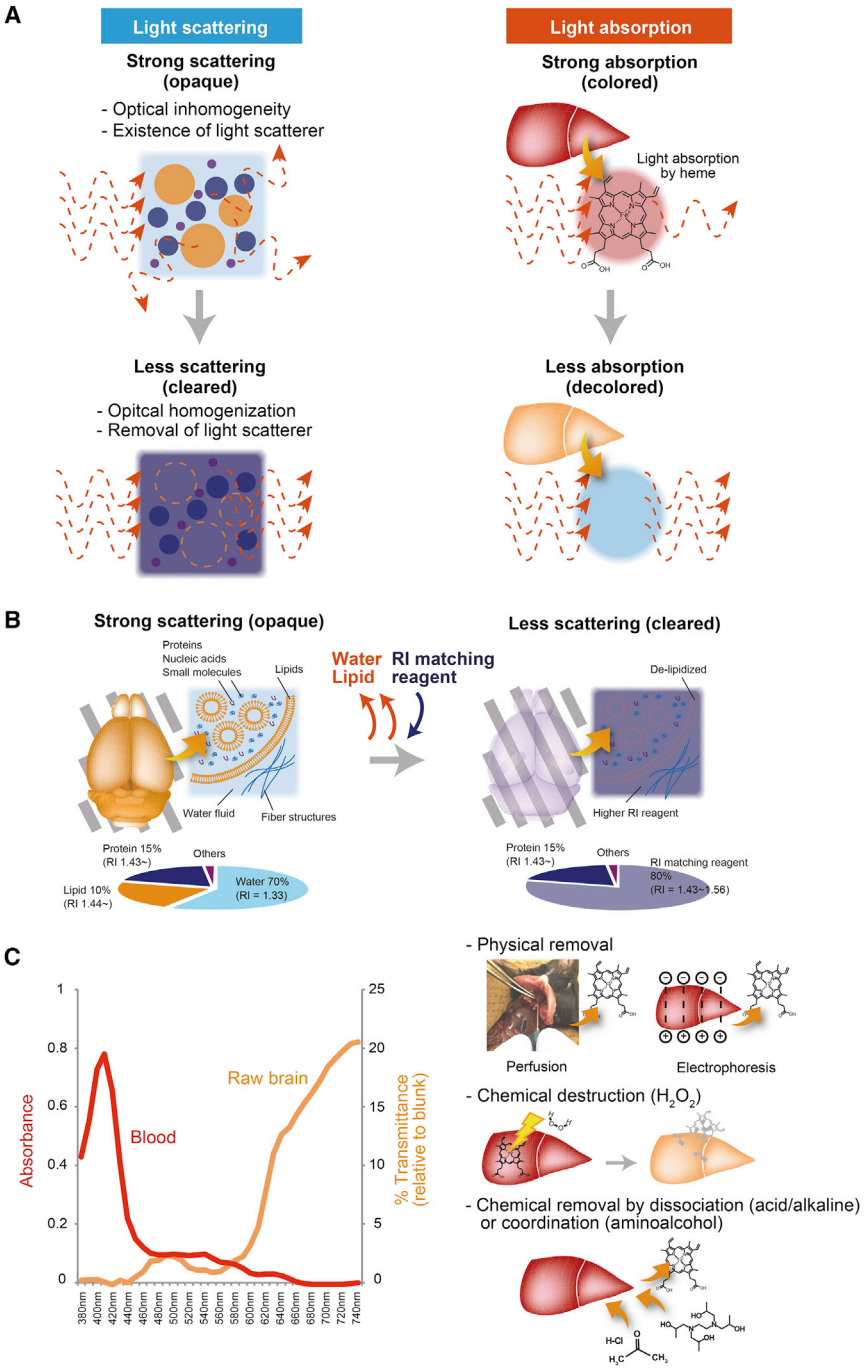

Figure 2. Strategies for Optical Tissue Clearing

(A) Two main steps contributing to tissue clearing. A biological tissue is composed of inhomogeneous materials with different optical properties, causing strong light scattering or absorption. Light scattering can be reduced by optically homogenizing the volumetric space with an RI matching reagent and removal of light scatterer (mainly lipid component). In addition, a major light absorber, heme in the tissue, should be removed to further tissue clearing.

(B) Light scattering reduction in the tissue. In the actual opaque tissue (e.g., brain), various components with different optical properties (represented as RI, for example) exist and construct some structures that work as light scatterers. Clearing can be achieved by removing water (lower RI) and lipid (higher RI) and fulfilling the space with RI-matching reagent (similar RI to the remaining components).

(C) Reduction of light absorption in the tissue. Blood has a light absorbing capacity under 600 nm of wavelength, which partly contributes to the reduction of light path in the raw (non-perfused) opaque tissue. Heme is the main light absorber in the blood and can be removed from tissue in several ways; heme-removal efficiency and protein preservation capability vary among the methods. The animal experiments were approved by the Animal Care and Use Committee of the RIKEN Kobe Institute and The University of Tokyo, and all of the animals were cared in accordance with the Institutional Guidelines.

sample so that light is transmitted straight in the forward direction. The refractive index (RI) is an index related to the velocity of light in a substance and reflects how much the speed of light gets attenuated as it passes through a material as compared to the speed of light in vacuum. In practical terms, RI is a simple indicator of optic properties and can be used to compare different systems. Discontinuity of RIs causes light scattering; inside a tissue, the light encounters inhomogeneity and areas of different RIs as well as different microscopic structures, all resulting in scattering and loss of light intensity in the forward direction (Figures 2A and 2B). Various tissue substances (e.g., proteins and lipids) have different RIs, and they are overall higher (around 1.4 to 1.6) (Johnsen and Widder, 1999; Tuchin, 2015) than surrounding water (1.33). Therefore, one reason why tissue optical clearing might work is that it would enable RI matching inside the sample; for example, when water in the sample is removed and then replaced with a substance of higher RI matched with the tissue's RI, light scattering is minimized and the tissue becomes more transparent. This RI matching concept was suggested by optics and examined in earlier studies (Liu et al., 1996; Tuchin, 2015; Tuchin et al., 1997). This concept was also considered in the development of most of the known tissue-clearing reagents. Indeed, the RI of these reagents is adjusted to around 1.4–1.5, similar to the gross RI range of several soft tissues (Bolin et al., 1989; Hama et al., 2015; Richardson and Lichtman, 2015). However, it is of note that the RI matching concept does not explain completely the reduction of light scattering observed. Choi et al. (2005), for example, cryopreserved human skin with tissue-clearing chemicals (a selected group of hydroxy-terminated reagents, organic solvents, and organic acids), and observed no correlation between RI and optic clearing potential. Mao et al. (2008) also investigated the clearing ability of alcohols

and concluded that the optical clearing effect is related to the number of hydroxyl groups rather than RIs. RI adjustment with inorganic ions (e.g., zinc iodide) was also found not to be effective for brain clearing (Ke et al., 2013). Such a discrepancy between the RI matching concept and some of the experimental observations can be attributed to other mechanisms of light scattering reduction. One explanation might be that in addition to affecting RI, clearing solvents also change the structure and size of biomolecules that scatter light. For example, sugars and sugar alcohols that are often used as components of clearing solutions destabilize and dissociate high-order collagen structures, which results in increased tissue transparency (Yeh and Hirshburg, 2006). Dehydration that occurs during clearing also contributes to the efficiency of the clearing process, beyond the fluid volume replacement by RI-adjusting reagents (Jiang and Wang, 2004; Rylander et al., 2006; Yu et al., 2011; Zhu et al., 2013). This process can make the tissue components denser, leading to more ordered structures and an increase in the particle size, which also reduces internal light scattering. A theoretical study also proposed that the light scattering is dependent on the particle size and shape in addition to the RI (Johnsen and Widder, 1999). Further plausible reasons, such as the penetration speed of the reagents into tissue, or matching of other optical properties between the reagents and surrounding tissue substances, can be also important. In conclusion, although there are solid practical solutions that allow for high clearing efficiency, more intensive studies of the chemical principles that underline tissue clearing are needed for us to fully rationalize empirical observations.

Modern tissue clearing reagents and protocols are summarized in Table S1. A tissue clearing protocol with an organic chemical cocktail (a mixture of benzyl alcohol and methyl salicylate) was first reported by a German anatomist Walter Spalteholtz more than 100 years ago (Spalteholz, 1914), and this protocol was still in use one century after it was first described (Steinke and Wolff, 2001). The original protocol was also modified to BABB (Murray's clear), a mixture of benzyl alcohol and benzyl benzoate that was used in whole-mount immunostaining and clearing as early as the 1980s (Dent et al., 1989), and later for whole-body fluorescent imaging of adult fly (McGurk et al., 2007) and mouse embryo with optical projection tomography (McGurk et al., 2007; Sharpe et al., 2002). The BABB was also used for the whole-brain fluorescence imaging of Thy1-YFP transgenic (Tg) mouse with light-sheet microscopy (Dodt et al., 2007). Other organic solvents were further screened in later studies for the purpose of higher clearing efficiency and fluorescence protein preservation. A protocol with dibenzylether (DBE) was found among these trials (Becker et al., 2012), and these protocols and imaging applications were summarized and proposed as 3D imaging of solvent-cleared organs (3DISCO) (Ertürk et al., 2012a) or shown to be compatible to whole-mount immunohistochemistry and following 3D imaging, reported as iDISCO (Renier et al., 2014). These methods were used for recent whole-organ imaging purposes, including rodent brain, spinal cord, kidney, lung, or embryo developments (Belle et al., 2014; Ertürk et al., 2012a, 2012b, 2014; Renier et al., 2014; Soderblom et al., 2015). During the clearing procedure, these organic reagents need complete dehydration to replace and fill the space in tissue. They immerse into the space, putatively making hydrophobic interactions with surrounding tissue components.

Biocompatible hydrophilic reagents have also been widely used; for example, the clearing ability of hydrophilic or water-soluble reagents, such as sugars (e.g., glucose), alcohols (e.g., glycerol, polyethylene glycol, butanediol, TMP, sorbitol, xylitol), DMSO, and oleic acid were tested in skin with the intention of medial application (Choi et al., 2005; Jiang and Wang, 2004; Mao et al., 2008; Vargas et al., 1999, 2001; Yu et al., 2011; Zimmerley et al., 2009). Biocompatible hydrophilic reagents can make hydrogen bonds with the tissue components together with the surrounding water, which is a milder interaction for biological materials than is the case with organic reagents. Therefore, various protocols with hydrophilic chemicals have been recently developed particularly for the purposes of fluorescence imaging. Generally, the hydrophilic reagents that can be dissolved in water at a very high concentration give a high RI in the solution and can thus be used for RI-matching reagents.

The sugar group are conventional tissue clearing reagents and have been adapted to some of the clearing protocols. For example, the SeeDB protocol uses a high concentration of fructose (~115% [w/v]) (Ke et al., 2013). Its RI was adjusted to ~1.49, an efficient value for brain clearing. This protocol maintained a constant sample volume during the procedure and preserved cellular morphology. The cleared sample was subjected to two-photon imaging with an optimized objective lens, covering the whole mouse brain area. A high concentration (~75% [w/v]) of sucrose was also tested for two-photon imaging of mouse cortex, reaching ~1.5 mm in depth (Tsai et al., 2009). Sucrose is also utilized in the CUBIC clearing protocol we developed, providing a chemical-based delipidation and RI-matching (Sca*l*eCUBIC-2, containing 60% [w/v] of sucrose to increase the RI to ~1.49, according to the evidence in the SeeDB study) (Susaki et al., 2014).

Alcohol group chemicals, such as glycerol, are also conventionally used for the tissue-clearing reagent. Sca*l*e, a urea-based clearing reagent, utilizes this chemical and achieves both RI-matching and swelling repression (Hama et al., 2011). The combination of alchohol group chemicals with CLARITY, a gel-embedding and SDS-based delipidation protocol, also gave a good clearing result (Epp et al., 2015). Aminoalcohols such as N,N,N′,N'-Tetrakis(2-hydroxypropyl)ethylenediamine and triethanolamine were adopted in CUBIC reagents by replacing glycerol in the original Sca*l*e recipe. Their efficient tissue-clearing ability was disclosed by a non-biased chemical screening in which all 7 aminoalcohols out of 20 polyhydric alcohol candidates showed the positive effect, suggesting that the structural characteristic is important (Susaki et al., 2014). A part of its clearing ability is attributable to RI matching (RI of 100% reagents = ~1.48), whereas they can also contribute to the other clearing processes, such as delipidation, by their weak detergent activity and alkaline-pH buffering ability. 2,2′-thiodiethanol (TDE), which has been shown to be useful as an RI-matching reagent, was shown in imaging of cultured cells (Staudt et al., 2007) and was recently used in deep 3D imaging and tested with mouse brains (Aoyagi et al., 2015; Costantini et al., 2015). Approximately sixty percent of TDE (RI = ~1.45) gives relatively good clearing performance with fluorescence preservation. This chemical was also tested as a final RI-matching reagent for

Please cite this article as: Susaki and Ueda, Whole-body and Whole-Organ Clearing and Imaging Techniques with Single-Cell Resolution: Toward Organism-Level Systems Biology in Mammals, Cell Chemical Biology (2016), http://dx.doi.org/10.1016/j.chembiol.2015.11.009

CLARITY in place of FocusCrear, a commercially available RI matching reagent (RI = 1.43–1.45), and supported whole-brain imaging with light sheet fluorescence microscopy (LSFM) (Costantini et al., 2015).

Sugar alcohols are also used for this purpose. Sorbitol, one of the conventional clearing reagents, was recently adopted in sRIMS (refractive index matching solution) (70% [w/v] Sorbitol, RI = ~1.44 by our measurement) and Sca*l*eS (40% [w/v] in Sca*l*eS4, RI = ~1.44) recipes because of its efficient clearing ability (Hama et al., 2015; Treweek et al., 2015; Yang et al., 2014). Poly-ether group molecules such as PEG are also used in the *Clear*^{T2} recipe (Kuwajima et al., 2013).

Urea, the main component of Sca*l*e reagents, was discovered as a clearing reagent due to its clearing ability of hydrophobic polyvinylidene floride (PDVF) membrane (Hama et al., 2011). However, tissue-clearing ability and PDVF-clearing ability do not seem correlated. A possible mechanism for the tissue-clearing ability of urea might be attributable to its hydration ability, which accelerates the penetration of water and other chemicals in the recipe and results in the decrease and subsequent matching of tissue's gross RI. The original Sca*l*e recipe has relatively low RI (1.38 in Sca*l*eA2), but an updated reagent obtained by adding sorbitol and DMSO has an increased RI value (~1.44) and improved clearing ability (Hama et al., 2011, 2015). Formamide apparently has chemical properties similar to urea and was applied to *Clear*^{T} recipes by single use or in combination with polyethylene glycol (Kuwajima et al., 2013).

Finally, some chemicals containing hydrophilic aromatic groups have been used as one of the clearing cocktail components. RIMS contains ~88% (w/v) of 5-(N-2,3-Dihydroxypropylacetamido)-2,4,6-triiodo-N,N'-bis(2,3-dihydroxypropyl)isophthalamide (Histodenz) (RI = 1.46, adjustable to RI = 1.38–1.48). A related chemical, diatrizoate acid, is applied to FocusClear™ (Chiang, 2002).

Minimization of Light Scattering by Active Removal

In addition to RI matching, an active removal of potent light scattering substances is effective for efficient tissue clearing (Figures 2A and 2B). In recent high-performance tissue-clearing methods, lipids are often removed because they are strong light scattering substances. Even in earlier studies, lipids were already suspected to be strong light scattering substances (Beuthan et al., 1996; Chance et al., 1995; Meyer, 1979; van Staveren et al., 1991). Due to their high RI range (around 1.5) (Beuthan et al., 1996; Tuchin, 2015) and property of producing granular structures (causing Rayleigh and Mie scattering), lipids are considered to be one of the main light scattering substances inside a tissue. Simple RI matching of lipid droplets and surrounding media was indeed correlated with reduced light scattering of the mixture (Chance et al., 1995; Wen et al., 2009). In addition, reagents and protocols with an active lipid removal property, including BABB and 3DISCO, which achieve this by employing organic solvents, CLARITY and its related protocols, or CUBIC, which uses physical lipid removal by electrophoresis or chemical lipid removal by high-concentration of detergents, generally result in a strong clearing efficiency (Chung et al., 2013; Costantini et al., 2015; Ertürk et al., 2012a; Hama et al., 2015; Richardson and Lichtman, 2015; Susaki et al., 2014; Yang et al., 2014).

Another major obstacle, particularly for whole-body imaging, is bone clearing. The mineral nature of the bones endows them with RI (1.55–1.65) that's higher than other tissues and surrounding substances (Ascenzi and Fabry, 1959; Ohmi et al., 2000). Administration of RI-adjusting reagents such as glycerol and propylene glycol partially reduced light scattering of bone (Genina et al., 2008). RI matching also improved imaging quality inside the bone, which was evidenced by infant brain imaging through the cranial bone (Tainaka et al., 2014) or application of BABB and 3DISCO for bisected femur clearing and imaging (Acar et al., 2015). As in the case of delipidation, RI-adjustment combined with a decalcification step further contributes to efficient clearing of bone-associated tissues. Chelating reagents such as EDTA or organic acids such as nitric, hydrochloric, formic, acetic, picric, or trichloroacetic acid are used in histological decalcification (Begum et al., 2010; Callis and Sterchi, 1998; Gomes et al., 2008). Recently, a passive CLARITY protocol (PACT) was combined with EDTA-based decalcification, leading to an efficient clearing and imaging of mouse tibia (PACT-deCAL protocol) (Treweek et al., 2015). Overall, integrated clearing protocols with finely tuned chemical compositions will continue to be developed in future studies to achieve better clearing results for whole-body imaging.

Minimization of Light Absorption by Active Removal

The process of light absorption is the transformation of light energy to some other form of energy as the light traverses the tissues, which eventually attenuates the intensity of the passing light (Tuchin, 2015). The light absorbing substances in the tissue should be thus removed for the subsequent imaging purposes in a process often referred to as decolorization. Such intrinsic light absorbing substances include lipid, beta carotene, lycopene, cytochrome *c*, and bilirubin, together with hemoglobin and melanin playing the dominant role due to their prevalance and their high light absorbing capacity. Heme in hemoglobin and myoglobin works as a major chromophore that absorbs visible light (Horecker, 1943; Weissleder, 2001) and causes reduction of visible light transmission (corresponding to ~0.1 of absorbance) in the blood (Figure 2C, left graph). This means that removal of hemoglobin is critical for whole-organ imaging of heme-rich tissues (Figure 2C, right panel). Conventionally, heme removal can be achieved using peroxide, a classicmethod for pigment bleaching that destroys the protein, and using acid-acetone or strong base wash, which leads to heme dissociation (Fagan et al., 1999; Kristinsson and Hultin, 2004; Oliver et al., 1987; Spalteholz, 1914; Steinke and Wolff, 2001). However, these protocols are too harsh to preserve cellular proteins, including GFP (Alnuami et al., 2008; Haupts et al., 1998; Steinke and Wolff, 2001), and are not widely used for fluorescence imaging.

Simple perfusion of buffer and fixative can contribute to the physical removal of red blood cells, and thus large amounts of heme, in the vessels; however, this is usually not enough for complete heme removal. A recent study showed the unexpected contribution of clearing reagent aminoalcohols in heme removal (Tainaka et al., 2014). The likely mechanism by which aminoalcohols remove heme is based on their ability to coordinate heme and replace the coordination point of the heme to globin protein chain due to its structural similarity. CLARITY and related protocols also have the ability to remove heme with their improved electrophoresis procedure, resulting in the preparation of almost completely decolored samples (Epp et al., 2015; Lee et al., 2014; Treweek et al., 2015).

Melanin, a pigment derived from tyrosine via a multistep reaction that includes oxidation and polymerization, is also an additional obstacle for tissue decolorization. Melanin granules are not only strong light absorbers but are also, given their size (in the range of 0.3–1 μm in the case of isolated human hair melanin granules [Potsch et al., 1997]) and high RI (1.6–1.7), strong light scatterers (Tuchin, 2015). The polymer-based structure of this molecule makes it insoluble in water and organic solvent. So far, no efficient protocol for melanin removal has been reported, and this remains an outstanding issue that requires further development in future studies.

Currently Available Protocols for Efficient Whole-Body and Whole-Organ Clearing

Protocols that achieve both lipid and heme removal as well as using RI matching reagents can make samples highly transparent. Most of tissue-clearing protocols using organic chemicals (BABB and 3DISCO) remove lipid components and make tissue samples clear by matching their RI values closely. Thus, these protocols can make various organs highly transparent (Belle et al., 2014; Ertürk et al., 2012a, 2012b, 2014; Renier et al., 2014; Soderblom et al., 2015).

The CLARITY-based protocol PARS (perfusion-assisted reagent release in situ) also seems to have both lipid and heme removing ability (Treweek et al., 2015; Yang et al., 2014). The CLARITY protocol includes a delipidation step by electrophoresis or by simple immersion in SDS, after which the sample is embedded in acrylamide gel to keep proteins and nucleic acids inside (Chung et al., 2013; Tomer et al., 2014; Treweek et al., 2015; Yang et al., 2014). In addition, an improved electrophoresis protocol can also remove most of the blood color within a tissue (Epp et al., 2015; Lee et al., 2014; Treweek et al., 2015). The delipidated and decolored organs are then immersed in RI-adjusting reagents such as FocusClear™ or RIMS (Chung et al., 2013; Treweek et al., 2015; Yang et al., 2014). In their attempt to achieve whole-body clearing of an adult mouse, Treweek et al. and Yang et al. perfused a body with SDS for up to 2 weeks after the gel embedding (PARS protocol) (Treweek et al., 2015; Yang et al., 2014). The cleared tissue obtained in this way can be also used for immunostaining and 3D imaging purposes.

The efficient whole-body clearing and imaging of an adult mouse was first demonstrated by the CUBIC protocol (Tainaka et al., 2014; Susaki et al., 2015). The CUBIC protocol also has the ability to delipidate tissue and decolorizeduring its tissue clearing. A nonionic detergent, Triton X-100, and possibly the aminoalcohol and urea as well, contribute to the delipidation. In addition, the aminoalcohol can actively remove heme from the tissue. These properties are important for the efficient whole organ/body clearing including heme-rich organs (Higashiyama et al., 2015; Susaki et al., 2015; Tainaka et al., 2014). CUBIC provides a whole-body clearing protocol by reagent perfusion and subsequent immersion, which clears whole infant and adult mouse bodies for up to 2 weeks and allows whole-organ/body imaging as well.

Preservation of Structural and Molecular Integrity after Clearing

One of the main issues with all the clearing strategies we described is that they all, to a certain extent, affect structural and molecular integrity of the sample under investigation. However, this is a recognized problem and there have been many efforts to provide practical solutions to minimize these artifacts. Shrinkage or swelling during or at the end of the clearing procedure may cause some artifacts in structural integrity. This point has been intensively examined in some clearing protocols such as SeeDB and Sca*l*eS. In general, clearing with organic reagents causes 20%–25% shrinkage of the sample (Table S2). Some of the hydrophilic chemical-based methods, such as Sca*l*eS, CLARITY, and CUBIC, render temporal expansion of clearing tissue (the size recovered to its original size after RI matching); however, such temporary swelling itself does not necessarily affect ultrastructures in EM section images (Hama et al., 2015; Mikula and Denk, 2015).

Delipidation-combined protocols (e.g., 3DISCO, CLARITY, CUBIC) can still target molecular to subcellular scales in addition to whole-organ to cellular scales, because subcellular structures (e.g., spines and axons) or molecular localizations (e.g., spine proteins) seem intact in the original papers (Chung et al., 2013; Ertürk et al., 2012b; Renier et al., 2014; Susaki et al., 2014). On the other hand, concerns about subcellular structural fidelity and molecular integrity were suggested in other studies. A recent study by Hama et al. examined the integrity of spine structures of the PACT, CUBIC, or 3DISCO-cleared brains by using electron microscopy and suggested a possible effect in the structures (Hama et al., 2015) while the original paper of CLARITY concluded that the ultrastructures were largely preserved (Chung et al., 2013). Because EM detects high electron density (mainly lipid structure) in the tissue, this type of microscope may not be compatible with such highly delipidated samples, and thus an optimized preparation and staining process should be considered (Chung and Deisseroth, 2013; Hama et al., 2015).

On the contrary, sample swelling can be utilized to get to improve the process of clearing and imaging. Expansion microscopy, a ''reverse-thinking'' method, oppositely exploited the tissue expansion to overcome the limit of optic resolution (Chen et al., 2015). This was achieved by embedding tissue into a hydropolymer, which led to a 4.5-fold linear expansion of the sample. A similar strategy was recently introduced in ePACT (Treweek et al., 2015).

Issues in molecular integrity (e.g., loss of molecules, quenching of fluorescent proteins, altered antigenicity) sometimes become a practical problem. A large part of proteins and nucleic acid seems to retain at the practically detected levels even after delipidation, because they can be still labeled and observed in the following staining. However, more quantitative evaluations evidenced that the delipidation steps indeed affects the amount of protein inside and the signal intensity of fluorescent proteins (Chung et al., 2013; Hama et al., 2015; Yang et al., 2014). Also, it should be noted that this process is inappropriate if lipid itself or lipophilic dyes are the observation target (Ertürk et al., 2012a; Hama et al., 2015) and thus different methods, such as adeno-associated virus (AAV) tracing, should be considered for a similar purpose.

Quenching of fluorescent proteins has been a particular focus in the history of tissue clearing and fluorescent imaging. This quenching can be caused by loss of the protein and destruction of its structure during the clearing step. Although the organic reagents give a strong clearing efficiency, fluorescent signal loss has been a main issue. Researchers have tried to ameliorate the problem by screening other hydration and RI matching chemicals, removal of peroxidase, or a change in the fixation method (Becker et al., 2012; Oldham et al., 2008; Sakhalkar et al., 2007;

 ©2016 Elsevier Ltd All rights reserved

Please cite this article as: Susaki and Ueda, Whole-body and Whole-Organ Clearing and Imaging Techniques with Single-Cell Resolution: Toward Organism-Level Systems Biology in Mammals, Cell Chemical Biology (2016), http://dx.doi.org/10.1016/j.chembiol.2015.11.009

CellPress

Schwarz et al., 2015b). In addition, usage of hydrophilic reagents mostly resolved this problem (Chung et al., 2013; Hama et al., 2011; Ke et al., 2013; Kuwajima et al., 2013; Susaki et al., 2014). The quenching is also dependent on treating temperature and pH—by controlling these parameters, GFP fluorescent signals were further preserved even in the BABB-based protocol (FluoClearBABB protocol) (Schwarz et al., 2015b). We also improved the Sca*l*eCUBIC-1 recipe based on this study, which significantly enhanced the fluorescent preservation property of the protocol (protocol available at http://cubic.riken.jp) Therefore, these parameters seem critical for keeping the molecular integrity of fluorescent proteins during clearing.

The antigenicity issue also relates to molecular integrity. Compatibility of various antibodies was examined in many clearing protocols (Belle et al., 2014; Chung et al., 2013; Ke et al., 2013) (Hama et al., 2011, 2015; Hirashima and Adachi, 2015; Renier et al., 2014; Susaki et al., 2014; Tainaka et al., 2014; Yang et al., 2014). Nevertheless, treatments with clearing reagents may affect the protein structure and alter antigenicity of the antibody target, as with the other histological treatments (fixation, cryopreservation, paraffin-embedding, or antigen-retrieval); for example, Hama and colleagues again reported the concern that some antibodies for synaptic and membrane proteins did not work well in the CUBIC sample (Hama et al., 2015). The opposite case may also exist because such compatibility is determined by the combination of antibodies and sample conditions. As is in the case with conventional immunohistochemical assays, it is important to check the compatibility of the specific antibody to the tissue after clearing treatments.

Additional Notes and Future Directions of Tissue Clearing

The proposed reagents and protocols discussed here can potentially be shuffled and combined to develop better protocols, based on their chemical classification and putative functions in the clearing process (Table S2). The strategy of combining and shuffling protocols has been explored, at least in part, and examples include combinations of TDE, SeeDB or Sca*l*eCUBIC-2 with CLARITY (Costantini et al., 2015; Susaki et al., 2014; Unnersjö-Jess et al., 2015), RIMS with CUBIC (Treweek et al., 2015), and SeeDB with Sca*l*e (FRUIT method) (Hou et al., 2015). Given the relatively small chemical space explored in tissue clearing studies, we argue that the field needs to invest effort in the discovery of other chemicals with higher clearing performance either among organic solvents or hydrophilic reagents. Non-biased comprehensive screening campaigns, similar to those used in the recently reported studies, are likely to help discover clearing reagents with different and unique chemical properties and structures (Kurihara et al., 2015; Susaki et al., 2014). We expect that hits identified using chemical screening will lead to further rational development of higher performing tissue-clearing reagents. Finally, in addition to the need to discover and develop new chemical reagents, we need to continue to investigate fundamental chemical principles of tissue clearing in order to place our understanding of how and why tissue clearing happens on stronger mechanistic footing (Cheong et al., 1990; Johnsen and Widder, 1999; Richardson and Lichtman, 2015; Tuchin, 2015; Wilson and Steven, 1990). Once we understand the mechanisms behind tissue clearing, we will be able to use that information to develop even more sophisticated technologies.

Cell Labeling Methods for Whole-Body and Whole-Organ Imaging

Tissue clearing and subsequent imaging are important aspects of the research scheme discussed here. One additional important step in this scheme is cell labeling, in which fluorescent tags or proteins are introduced to enable visualization of different cellular types, components, and activities. Here, we will summarize recent progress in multi-color fluorescent imaging with various fluorescent proteins and small molecule tags and discuss (Figure 3).

Cell Labeling with Fluorescent Proteins

One of the major ways to accomplish cell labeling is through the use of fluorescent proteins (Figure 3A). Here, one or more fluorescent proteins are introduced into a genome, usually fused to the target protein of interest or to its promoter region, and allowed to express. The imaging method is then optimized to measure the fluorescent signal of these proteins. This means that it is critical to preserve structural integrity of the fluorescent proteins, and several tissue-clearing methods were optimized to preserve the fluorescent protein signals.

In general, the first step toward the robust fluorescent signal is ensuring that fluorescent protein(s) used are expressed at appropriate levels. Cell-type specific promoters and enhancers are usually used to dissect a specific, genetically defined population of cells (Huang and Zeng, 2013; Luo et al., 2008). Furthermore, to achieve both specificity and high expression level simultaneously, a binary expression system (a combination of *driver*, determining the cell specificity, and *reporter*, turned on by the driver activity and expressed under a strong and ubiquitous promoter) is applied. In experiments with mammals, the bacteriophage Cre recombinase, Yeast flippase (Flp), or bacterial tetracycline-regulated transactivator (tTA) system are widely used as the drivers. They are applied not only for the simple driver-reporter combination, but also for more sophisticated genetic labeling methods. For example, combinations of Cre-Flp, Cre-tTA or split Cre molecules realize the intersection or subtraction of reporter expression (Huang and Zeng, 2013). Brainbow (Cai et al., 2013; Livet et al., 2007) and mosaic analysis with double markers (MADM) (Zong et al., 2005) allow distinct and isolated cell labeling by multiple color variation, which also rely on Cre recombinase activity. However, whole-organ/body imaging has not yet been tried for these samples.

Inclusion of subcellular-scale connectivity information in a single whole-organ/body dataset is still challenging, but several genetic tools can be applied for such purposes. For investigating synaptic connectivity with light microscopy, Kim and colleagues developed mammalian GFP reconstitution across synaptic partners (mGRASP) (Kim et al., 2012). GRASP is based on functional complementation between two non-fluorescent split-GFP fragments. When these fragments are tethered to the synaptic cleft in two different, synaptically connected neurons, the fluorescent signal will be observed only if the two neurons are in a close proximity, which allows the two non-fluorescent GFP fragments to come together and form the complete and fluorescent GFP. In this case, a Cre recombination system was used to label pre- and post-mGRASP cells.

Please cite this article as: Susaki and Ueda, Whole-body and Whole-Organ Clearing and Imaging Techniques with Single-Cell Resolution: Toward Organism-Level Systems Biology in Mammals, Cell Chemical Biology (2016), http://dx.doi.org/10.1016/j.chembiol.2015.11.009

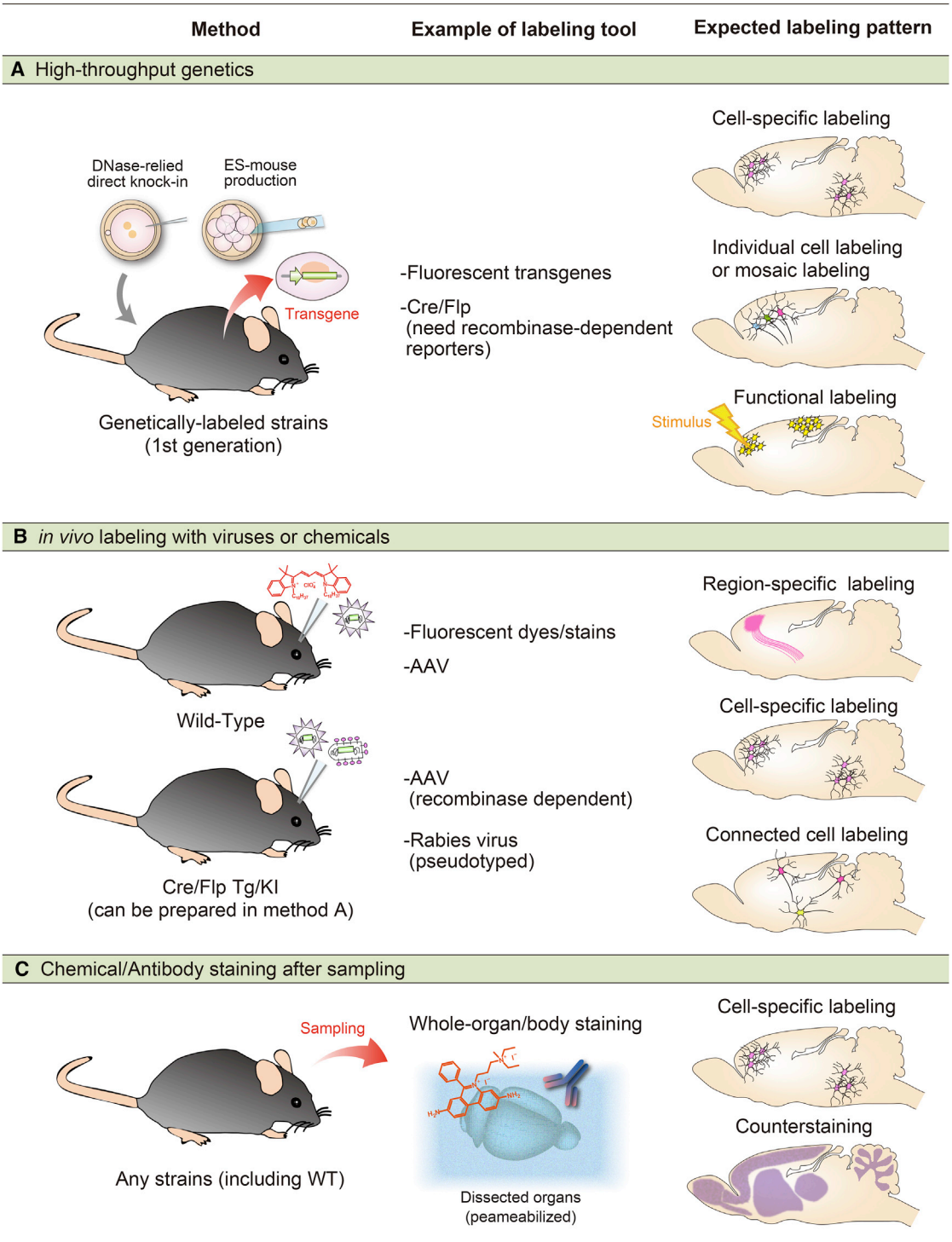

Figure 3. Strategies for Cell Labeling

Cells should be properly labeled according to their biological context in the system, such as variation, structure, or function. This can be achieved by the following steps.

(A) Genetic introduction of fluorescent markers or recombinases. These procedures have conventionally taken sigificant time and effort. However, most of the mating procedures can be skipped by using recent high-throughput mouse genetics technologies.

(B) In vivo labeling of cells or regions with chemicals (e.g., neural tracer) or viruses.

(C) Whole-mount histochemical procedures with chemical stains and antibodies. For efficient 3D staining, a permeabilization step is apparently needed.

 ©2016 Elsevier Ltd All rights reserved

Please cite this article as: Susaki and Ueda, Whole-body and Whole-Organ Clearing and Imaging Techniques with Single-Cell Resolution: Toward Organism-Level Systems Biology in Mammals, Cell Chemical Biology (2016), http://dx.doi.org/10.1016/j.chembiol.2015.11.009

Functional labeling of cells and their time-series observation are critical for understanding dynamical properties of the multicellular systems. Promoters and enhancers of immediate-early genes (IEGs), a group of genes that are induced immediately by neuronal activity, have been widely used to achieve this goal (Huang and Zeng, 2013; Kawashima et al., 2014). These genetic tools label the integrated neural activities within several minutes to hours, on the timescale that is also proper for a tissue clearing and imaging scheme. Several related tools are also available for whole-brain functional labeling at the cellular resolution. In these cases, a few things that should be considered are promoter and enhancer types, which should be chosen depending on the cell type and desired signal intensity. For these purposes, the regulatory elements of *c-Fos* and *Arc*/*Arg3.1* are widely used. An isolated *c-Fos* promotor successfully labeled a wide range of neurons activated by pentylenetetrazol or kainic acid in vivo (Schilling et al., 1991; Smeyne et al., 1992) and was later utilized in *c-Fos*-GFP transgenic animals (Barth et al., 2004; Cifani et al., 2012). Whole-brain *c-Fos*-GFP expression was monitored with serial two-photon tomography, revealing social behavior-induced neural evoking patterns in male and female mice (Kim et al., 2015b). *Arc*-GFP Knock-in (KI) and Tg, or *Arc*-Venus Tg animals were also established for the similar purpose (Eguchi and Yamaguchi, 2009; Grinevich et al., 2009; Vousden et al., 2015; Wang et al., 2006). The latter Tg strains have been evaluated in a whole-brain 3D imaging with CUBIC (Susaki et al., 2014) and serial two-photon tomography (Vousden et al., 2015). Kawashima and colleagues identified a neuronal activity–dependent enhancer of an *Arc* gene promoter, the synaptic activity–responsive element (SARE), and developed a genetic tool for labeling in vivo neural activity by using a synthetic, enhanced SARE (E-SARE) promoter (Kawashima et al., 2009, 2013). *c-Fos*-tTA, *Arc*-CreER (tamoxifen-induced Cre) Tg, or the TRAP system were further developed to restrict the time window of functional cell labeling (Denny et al., 2014; Guenthner et al., 2013; Reijmers et al., 2007). In those systems, the fluorescent transgene is only induced after or during the time window of doxycycline or tamoxifen administration, but once labeled, the expression can be sustained until observation. For shorter timescales, immunostaining of phosphorylated extracellular signal-regulated kinase (ERK) has been also used (Cancedda et al., 2003; Randlett et al., 2015).

Virus vectors are another widely applied way to deliver genetic tools into animals (Huang and Zeng, 2013; Luo et al., 2008) (Figure 3B). For the specific cell labeling, viruses with a Cre/Flp/tTA-driven expression cassette are usually injected in the driver KI or Tg strain (again, high-throughput mouse genetics are important here!). Furthermore, an engineered tropism, the specificity of virus for a particular cell or tissue, helps a specific, cell-type-dependent infection of pseudo-typed virus vectors. Several engineered viruses, including AAV, lentivirus, retrovirus, rabies virus (RV), canine adenovirus (CAV), or herpes simplex virus are in use.

Systematic projection mapping of neurons (or projectome) was performed with AAV and whole-brain 3D imaging. A large-scale mesoscopic connectome project by the Allen Institute is a representative study, performing comprehensive AAV labeling and serial two-photon tomography imaging (see below) (Oh et al., 2014). Furthermore, AAV-based Brainbow tools can be utilized for similar experiments to examine the single-cell level connectivity (Cai et al., 2013). A recent effort to improve AAV capsid (PHP.B) supports more efficient expression in global neural areas (Deverman and Patterson, 2015).

The RV system is also widely used for comprehensive neural input mapping. RV infects neurons through axon terminals and is spread by retrograde transsynaptic transfer. The RV system, which was developed by limiting pre-synaptic infections of the virus to the single *trans* spreading and engineered by harboring the pseudo-type envelope, provides the cell-type specific infection and direct input mapping of neural circuit or even input-output mapping with CAV (TRIO method) (Osakada and Callaway, 2013; Schwarz et al., 2015a; Wickersham et al., 2007). The macroscopic to mesoscopic resolution of whole-organ imaging is suitable for detecting the RV-labeled cells in a high-throughput and comprehensive manner. Indeed, automated serial sectioning (Velez-Fort et al., 2014) or multiple whole-brain imaging with tissue clearing (Lerner et al., 2015; Menegas et al., 2015; Niedworok et al., 2012; Schwarz et al., 2015b) has been recently performed for this purpose.

Several large resource institutes systemically produce and provide many driver strains and support the use of these genetic tools by making them available to the community (e.g., GENSAT [Gerfen et al., 2013; Gong et al., 2007] and the Allen Institute [Madisen et al., 2010]). However, it is also critical for each researcher to produce new KI or Tg strains in a high-throughput manner. The recently developed technologies of genome editing and developmental engineering enable such high-throughput production of new KI or Tg strains (Figure 3A). The CRISPR-Cas system, an RNA-guided nuclease technology, is one of the representatives (Cong et al., 2013). Reporter knocked-in animals can be directly produced at the rate of ~45% by injecting Cas9 RNA, guide RNA, and a targeting construct with a transgene into fertilized eggs (Aida et al., 2015; Yang et al., 2013). Another example is the ''ES-mouse'' technology. ES-mouse refers to an F0 generation animal with almost all bodies composed of the injected ES cell-derived cells (the animal is also called ~100% chimera mouse). The efficient production of ES-mouse was achieved by the usage of 8-cell stage embryos (all cells are still totipotent) and the ground-state ES cells cultured with several inhibitors (Kiyonari et al., 2010; Poueymirou et al., 2007; Ying et al., 2008). Both technologies significantly shorten the period to generate a new KI or Tg strains because a new mouse strain can be generated directly from genome-edited fertilized eggs or ES cells within a single generation, without mating. Thus, researchers can complete their experiments with the first generation animals from the genome-editing process (typically within 2–4 months). This strategy has already been shown in knockout phenotyping (Poueymirou et al., 2007) and the production of a new knock-in strain harboring a bright red fluorescent protein transgene (Susaki et al., 2014; Tainaka et al., 2014).

Cell Labeling with Small Chemicals and Antibodies

Histological tissue staining with small molecule reagents and antibodies can be used to detect specific molecules, structures, and cell types inside tissue, even for 3D samples (Figure 3C). For example, whole-mount immunostaining with BABB was performed even in earlier studies by using embryos of frog, opossum, and mouse, or mouse cerebellum after weaning (Dent et al., 1989; Luque et al., 1998b; Sharpe et al., 2002; Sillitoe

Please cite this article as: Susaki and Ueda, Whole-body and Whole-Organ Clearing and Imaging Techniques with Single-Cell Resolution: Toward Organism-Level Systems Biology in Mammals, Cell Chemical Biology (2016), http://dx.doi.org/10.1016/j.chembiol.2015.11.009

and Hawkes, 2002). Modified Golgi-Cox and Nissl staining were also performed for uniform whole-brain staining of rodents (Wu et al., 2014; Zhang et al., 2011). Most of the recent clearing and imaging technologies are compatible with such whole-mount staining or pre-labeling before imaging. However, the procedures still have some difficulties, particularly because of the penetration step into deep regions of 3D tissue.

Fluorescent small compounds have been widely used in clearing and imaging studies; for example, many nucleic acid stains (e.g., DAPI, propidium iodide, SYTO series dyes, TO-PRO3, or DRAQ5) are important for giving anatomical orientations during and after observation (Costantini et al., 2015; Susaki et al., 2014; Yang et al., 2014). This is even informative for some specific structures inside the tissue, as evidenced by extraction or quantitative comparison of coronal vessels in the heart, bronchial tracts in the lung, or ducts and islets of Langerhans in the pancreas (Tainaka et al., 2014). This also gives a global anatomical cue for calculating registration and alignment parameters of whole-brain analysis (Susaki et al., 2014, 2015). Fluorescent Nissl stain reagents (NeuroTrace) (Yang et al., 2014) can be also used for a similar purpose. Lipophilic tracing dyes (e.g., DiI) can be introduced in live animals (Figure 3B) and are compatible with some tissue clearing protocols (Hama et al., 2015; Hou et al., 2015; Ke et al., 2013; Kuwajima et al., 2013). However, preservation of lipid contents should be considered in the usage of such chemicals. Indeed, protocols with delipidation (e.g., CUBIC, 3DISCO, PACT) are not apparently amenable to the use of these lipophilic dyes (Ertürk et al., 2012a; Hama et al., 2015). Fixable protein tracers such as *Phaseolus vulgarism* leucoagglutinin and cholera toxin subunit b or dextran-base tracers (e.g., FluoroRuby) can substitute for the similar tracing purpose, even in the whole-brain scale (Quinta et al., 2015; Zingg et al., 2014).

Immunohistochemical analysis with various antibodies and subsequent 3D imaging is compatible and benefits from many clearing protocols (Belle et al., 2014; Chung et al., 2013; Hama et al., 2011, 2015; Hirashima and Adachi, 2015; Ke et al., 2013; Renier et al., 2014; Susaki et al., 2014; Tainaka et al., 2014; Yang et al., 2014). The permeabilization step is critical for antibody penetration in the 3D tissue sample. Delipidation by highly concentrated detergents or electrophoresis substitutes for this step and supports staining of several millimeters in depth (Chung et al., 2013; Susaki et al., 2014; Tainaka et al., 2014; Tsai et al., 2009; Yang et al., 2014). These samples were observed after clearing with high-concentrated sucrose, CLARITY, or CUBIC protocols. MeOH and/or DMSO with hydrogen peroxide (for pigment bleach and endogenous peroxydase destruction, in the original paper) or with repeated freeze-thaw procedure are also conventionally used (Davis et al., 1991; Dent et al., 1989; Luque et al., 1998a; Sillitoe and Hawkes, 2002). The dehydration-rehydration procedure permeabilize the sample possibly by removing membrane lipids, which enabled the whole-mount immunostaining and 3D imaging of mouse hemisphere, whole mouse embryo and postnatal infants, and adult mouse organs such as the brain and the kidney (Gleave et al., 2013; Renier et al., 2014). The samples were cleared with BABB or 3DISCO (proposed as ''iDISCO'' protocol) for 3D imaging. iDISCO also provides an alternative permeabilizing procedure with 20% DMSO and low-concentration (0.1–0.2%) of detergent cocktails to keep antigenicity. AbSca*l*e and ChemSca*l*e protocol, recently reported by Hama and colleagues, is unique in utilizing urea before and during 3D staining (Hama et al., 2015). In this protocol, the tissue is first permeabilized with several Sca*l*e reagents (Sca*l*e S0, A2 and B4, containing 4–8 M urea and low concentrations of lipid removal reagents) and then antibodies or chemicals react in a solution containing urea again.

Large samples including whole adult mouse brain, heart, lung, stomach, or intestine were tried for 3D immunohistochemistry (Chung et al., 2013; Renier et al., 2014; Tainaka et al., 2014). However, the penetration depth had not been fully evaluated in these studies. Recently, antibody penetration depth was evaluated in Sca*l*eS study by comparing the staining degree of NeuN antibody in pre-cut and post-cut samples (Hama et al., 2015), showing uniform staining of mouse hemisphere. To further improve the whole organ/body staining and imaging, factors affecting penetration rate should be covered in detail. Studies suggested some critical factors; for example, Li et al. investigated diffusion of antibodies in a CLARITY-cleared sample and showed the diffusion is well described by Fick's law (Li et al., 2015), which suggests that several factors such as particle radius, concentration of stains, penetration time, or interactions between stains and the sample are important. Indeed, the diffusion coefficients of IgG, $F(ab')_2$, Fab, or nanobody are smaller ($\sim$1/4) than that of the small molecule components of the solution. Furthermore, it takes IgG (150 kDa) about ten times longer to achieve the same degree of penetration as a nanobody (14 kDa). The importance of a stain's concentration was examined in the iDISCO study, showing that the 3D staining results of kidney were much improved when using more concentrated antibody preparation (Renier et al., 2014). In addition to factors on the stain side, physicochemical properties of the tissue further complicate the issues in 3D staining; for example, lower PFA concentration, protease K treatment, and the repeated freeze-thaw cycle improved the antibody penetration by apparently affecting the mesh size of the sample (Gleave et al., 2013; Luque et al., 1998a). Solving these issues and developing more sophisticated 3D staining protocol is an active area of research. For example, a method that employs external electric field enables the active transport of stains and achieves rapid labeling of mouse organs with stains that vary from small molecules to antibodies within 1 day (Kim et al., 2015a; Li et al., 2015).

In addition to small molecule and antibody stains, whole-mount FISH protocols were also tried. However, more improvement is needed for its practical use in 3D staining and imaging (Luque et al., 1998a; Yang et al., 2014).

3D Fluorescence Imaging for Whole-Body and Whole-Organ Cell Profiling

Criteria for Whole-Body and Whole-Organ Imaging with Single-Cell Resolution

Technically speaking, the goal of the imaging step is to take whole-organ/body images with a reasonable (cellular to subcellular) resolution in a high-throughput manner. Instruments used for this purpose are summarized in Table S2. There are several critical points to be considered to ensure high quality performance of the imaging step. The imaging color should be properly selected according to the imaging purposes. For example, particularly in the case of deeper 3D imaging, brighter

 ©2016 Elsevier Ltd All rights reserved

Please cite this article as: Susaki and Ueda, Whole-body and Whole-Organ Clearing and Imaging Techniques with Single-Cell Resolution: Toward Organism-Level Systems Biology in Mammals, Cell Chemical Biology (2016), http://dx.doi.org/10.1016/j.chembiol.2015.11.009

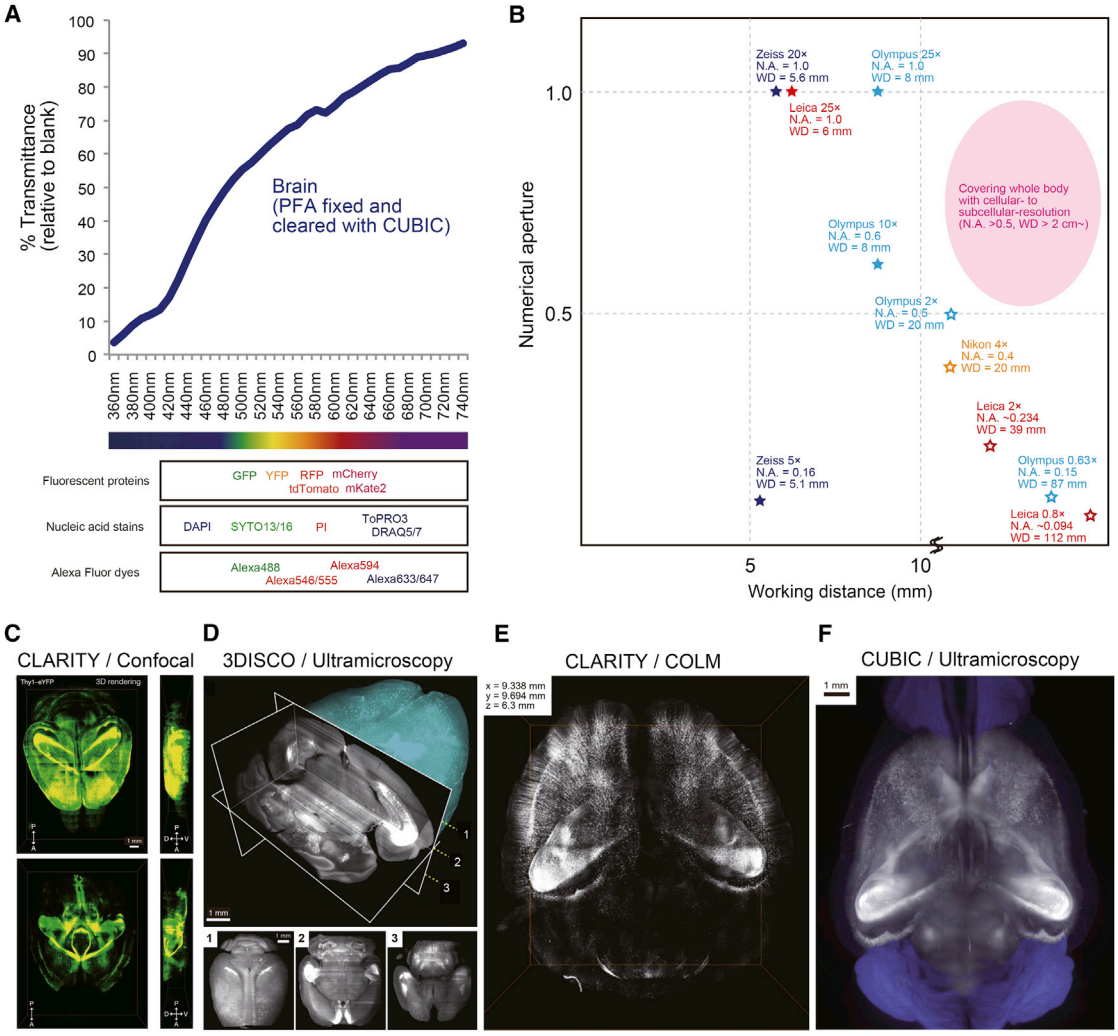

Figure 4. Imaging Strategies and Examples of Whole-Brain Imaging

(A) Choice of color. Even after optical clearing of tissue, red light can penetrate more than blue to green light, and imaging quality can be better when red fluorescence is used. Typical fluorescent proteins or dyes are shown for reader's reference. The graph of percentage of transmittance was re-plotted from the data in Susaki et al., 2014.

(B) Choice of objective lens. For whole-organ/body imaging with cellular (several microns)-to-subcellular (<1 μm) resolution, an ideal objective lens would have a significant optical resolution (e.g., Rayleigh resolution is approximately 0.67 μm when N.A. = 0.5, λ = 0.55 μm), and a deep working distance (e.g., ~20 mm for the half-depth of an adult mouse body). In the current microscopy setups (Table S2), longer WD with a lower N.A. lens for wide-field imaging or shorter WD with a higher N.A. for higher resolution imaging are typically adopted. Lenses in the figure are: XLPLN10XSVMP, XLSLPLN25XGMP, MVPLAPO0.63X, MVPLAPO2X (Olympus); MacroFluo Planapo 0.8 × and 2 ×, HC FLUOTARL 25 × (Leica); Z.1 detection optics 5 ×, LD Plan-Aphochromat 20 × (Zeiss); and AZ-Plan Apo 4 × (Nikon). Lined and fulfilled stars indicate dry and immersion objectives, respectively.

(C–F) Examples of whole-brain 3D imaging of Thy1-GFP/YFP Tg strains, with various imaging setup. Images were adapted with permission from Chung et al., 2013, for (C), Ertürk et al., 2012a, for (D), and Tomer et al., 2014, for (E), respectively. The image in (F) was recaptured from data in Susaki et al., 2015.

The animal experiments related to (A) and (F) were approved by the Animal Care and Use Committee of the RIKEN Kobe Institute and The University of Tokyo, and all of the animals were cared in accordance with the Institutional Guidelines.

fluorescent signals of red to near infrared wavelength can give better results due to their higher penetration in the tissue (Figure 4A). Also, the optical resolution of the images should be properly selected. This is mainly determined by the numerical aperture (N.A.) of the objective lens for x-y, where sub-micrometer range can be achieved when N.A. of the objective is over 0.34~ according to the Rayleigh criterion of the optical resolution, 0.61 × λ/N.A., where λ is the wavelength of light (λ = 0.55 μm is typically used). At low magnification range, such as a macro imaging setup, the camera's pixel size (*p*) and magnification (*M*) of objective determine the final x-y resolution of the image, 2 × *p*/*M*. Furthermore, for the 3D imaging purpose of a large sample, working distance (WD) of the objective is also critical. The need for trade-offs between N.A. and WD in the currently available objectives (Figure 4B), the field-of-view size and magnification of objective, and the pixel size and camera sensitivity, can be minimized by improvement of devices or sample preparation to allow for better scalable imaging. For example, a recent idea to combine Expansion microscopy and ePACT can overcome the optical resolution by expanding the sample itself

Please cite this article as: Susaki and Ueda, Whole-body and Whole-Organ Clearing and Imaging Techniques with Single-Cell Resolution: Toward Organism-Level Systems Biology in Mammals, Cell Chemical Biology (2016), http://dx.doi.org/10.1016/j.chembiol.2015.11.009

(Chen et al., 2015; Treweek et al., 2015). The z-resolution is determined by the thickness of optical or physical sectioning, which is dependent on the instrument (see below). Lastly, the throughput also depends on the specifications of imaging instruments (e.g., way of illumination, field-of-view size, or speed of stage movement) and signal intensities from the sample.

Currently available instruments tend to be built for a range of resolution and throughput according to the experimental purposes (Table S2), from a lower resolution with a wide field-of-view (e.g., a whole mouse horizontal image in a single x-y image) to a higher resolution (e.g., reconstitution of long-range axons in the volumetric image). Even in the former setup, imaging with a single cell resolution can be achieved using sparsely labeled targets such as *Arc* promoter-driven fluorescent proteins or RV-labeled neurons (Schwarz et al., 2015b; Susaki et al., 2014; Susaki et al., 2015). On the other hand, the latter setup requires image reconstitutions by tiling or stitching. Open-source computational tools like XuvTools (http://www.xuvtools.org [Emmenlauer et al., 2009]) or TeraStitcher (http://abria.github.io/TeraStitcher/ [Bria and Iannello, 2012]) are available for such calculation, while the data size, resolution and image acquisition, and calculation times are also the trade-offs. These instruments and imaging applications are further discussed in the following sections.

LSFM for High-Throughput Imaging with Single-Cell Resolution

Optical sectioning of highly transparentized samples obviates the need for serial sectioning and reconstitution and provides a high-throughput approach for globally mapping cells and cell populations across the organs and body (Chung and Deisseroth, 2013; Luque et al., 1998b). A combination of two old-yet-new technologies, tissue clearing and LSFM, is fruitful in this aspect and has been rapidly growing within the latest decade (details were recently reviewed in Keller and Ahrens, 2015). A thin light sheet is illuminated from the side of a transparent specimen to obtain optical sectioning without physical sectioning, and excitation signals are acquired from its vertical sides. Because excitation-detection paths are separated, and a single x-y plane image is acquired in a single sweep (without line scanning), this microscopy instrument enables high volumetric imaging speed, high signal-to-noise ratio, and low levels of photobleaching and phototoxic effects (Keller and Ahrens, 2015; Keller and Dodt, 2012; Osten and Margrie, 2013; Tomer et al., 2014). These advantages meet the requirements for the systems biology approach, as they achieve coverage of a wide range of spatial and temporal scales. Various related experiments in recent years have utilized this microscopy for whole-organ and whole-organism imaging purposes, including spatiotemporal monitoring of animal embryo developments (Keller et al., 2008; Krzic et al., 2012; Tomer et al., 2012; Truong et al., 2011; Wu et al., 2011, 2013), functional imaging of whole-brain neural activities in fish and fly brains (Ahrens et al., 2013; Lemon et al., 2015; Panier et al., 2013; Vladimirov et al., 2014), whole-organ imaging of dozens of samples in a realistic timescale (Lerner et al., 2015; Menegas et al., 2015; Susaki et al., 2014; Tainaka et al., 2014), or even whole infant mouse imaging at the cellular resolution (Tainaka et al., 2014).

Development of the light sheet microscopy dates back to the work of Siedentopf and Zsigmondy done at the turn of the twentieth century (Siedentopf and Zsigmondy, 1903). The first attempts to combine light sheet microscopy with tissue clearing were reported in early 1990s by Voie and colleagues, who used rhodamine-immersed guinea pig cochlea and Spalteholz's clearing mix (Voie et al., 1993). More recently, Dodt and colleagues used ultramicroscopy, an instrument with macro-zoom microscopy and a light-sheet illumination unit to take a large field-of-view image to acquire images of YFP-expressing mouse brain cleared with BABB (Dodt et al., 2007). The related LSFMs were later used in 3DISCO applications and CUBIC studies (Figures 4D and 4F, Table S2) (Belle et al., 2014; Ertürk et al., 2012a, 2012b, 2014,; Renier et al., 2014; Soderblom et al., 2015; Susaki et al., 2014; Tainaka et al., 2014). Furthermore, several research teams developed a custom-build LSFM for whole-organ imaging of BABB or CLARITY samples (Figure 4E and Table S2) (Costantini et al., 2015; Lerner et al., 2015; Niedworok et al., 2012; Schwarz et al., 2015b; Tomer et al., 2014). Recently, a commercially available LSFM was also utilized for a large-scale data collection (77 specimens) of RV-labeled brains (Menegas et al., 2015) (Table S2).

Because the sample should be highly transparentized, some of the recent tissue-clearing protocols (3DISCO, CLARITY, or CUBIC, so far) are mainly applied to the large volumetric imaging with LSFM. In addition, some issues related to the optic configuration should be considered: one is the axial resolution, which is determined by the minimum thickness of the sheet and its cross-section shape. The thickness of the illumination beam is non-uniform and is transverse to the imaging axis, having a "waist" at the thinnest part (Leischner et al., 2009; Voie et al., 1993). This is because the illumination beam is focused by a cylindrical lens or an objective lens in the illumination path. Furthermore, the confocal parameter, a value related to the width of light sheet waist, becomes shorter according to the square of half-sheet thickness, assuming a Gaussian beam. This non-uniformity of the sheet causes different z-resolution throughout the image, particularly in a large field of view and with a thinner sheet. A proper range of parameters among the minimum sheet thickness, x-y resolution, and field-of-view size should be thus selected. This problem can be avoided by merging signals obtained only from the beam waist (Buytaert and Dirckx, 2007; Santi et al., 2009), but this is done at the expense of imaging throughput. Other attempts to improve the axial resolution or image contrasts of LSFM are focused on developing additional LSFM configurations for various imaging purposes, exploiting a virtual-slit effect by rolling shutter mode of a sCMOS camera chip (Baumgart and Kubitscheck, 2012; Tomer et al., 2014), multiview deconvolution using the images of isotropic multiview LSFM (Chhetri et al., 2015), combinatorial use of confocal system (Silvestri et al., 2012), light sheet produced by incoherent extended focusing (Dean and Fiolka, 2014), Bessel-beam illumination (Fahrbach and Rohrbach, 2012; Fahrbach et al., 2010; Planchon et al., 2011), two-photon illumination (Planchon et al., 2011; Truong et al., 2011; Zong et al., 2015), structured-illumination (Kalchmair et al., 2010; Keller et al., 2010), lattice light sheet (Chen et al., 2014), or stimulated emission depletion (STED)-integrated light sheet (Friedrich et al., 2011), some of which were already tested for whole-organ/body imaging in a scalable manner (Table S2). Furthermore, deconvolution or adaptive optics was also introduced for improving image quality (Dodt et al., 2007; Ertürk et al., 2012a;

 ©2016 Elsevier Ltd All rights reserved

Please cite this article as: Susaki and Ueda, Whole-body and Whole-Organ Clearing and Imaging Techniques with Single-Cell Resolution: Toward Organism-Level Systems Biology in Mammals, Cell Chemical Biology (2016), http://dx.doi.org/10.1016/j.chembiol.2015.11.009

CellPress

Tainaka et al., 2014; Turaga and Holy, 2010), but should overcome the vast amount of calculation in the current situation.

In summary, LSFM application for cleared tissue imaging provides one of the best opportunities to acquire multiple 3D images in a high-throughput manner. Some of the recent studies have started to use this strategy to address specific biological question. Further development and optimization of the instruments will provide multi-scale imaging options, from sub-cellular to whole-organ/body scales.

Other Microscopy Setups

Several tissue-clearing methods were also combined with confocal and multi-photon imaging techniques. Although there are some drawbacks, such as photobleaching and much longer acquisition time, these applications provide more opportunities for large and deep 3D imaging experiments.

While single-photon confocal microscopy approaches are limited to use near the opaque tissue surface (~100 μm) (Helmchen and Denk, 2005), efficient tissue clearing enabled sub-millimeter to millimeter scale observations (Calve et al., 2015; Hama et al., 2011, 2015; Ke et al., 2013; Renier et al., 2014; Susaki et al., 2014; Unnersjö-Jess et al., 2015; Yang et al., 2014) and even whole-brain, whole-lung, and whole-embryo imaging (Chung et al., 2013; Quinta et al., 2015) (Figure 4C and Table S2). A combinatorial use of wide-field LSFM for whole-organ observation and confocal microscope with higher N.A. objectives will further allow a scalable observation in a single specimen, avoiding quenching and longer scanning time. Two-photon microscopy allowed imaging of several hundred microns to 1 mm in depth in various non-cleared organs by the use of a far-red pulse laser, which generates signals in a non-linear fashion (Helmchen and Denk, 2005). Again, by combining two-photon microscopy with tissue clearing, it was possible to conduct an imaging experiment covering whole-brain areas (Ke et al., 2013). In this case, a moderate clearing efficiency, which preserves the ultrastructures, is sufficient for such two-photon imaging application.

Optic projection tomography (OPT) is another imaging setup that is used with optic tissue clearing. OPT provides the opportunity for rapid, bright-field, and fluorescent 3D imaging of even centimeters cubed in size with a few micron resolution (Wong et al., 2013) (Table S2). When combined with BABB clearing, large volumetric samples, including developing mouse embryos, xenograft tumor tissues, whole mouse heart, kidney, brain or hemisphere, and white adipose tissue have all been examined successfully using OPT (Anderson et al., 2013; Gleave et al., 2012, 2013; Jeansson et al., 2011; Oldham et al., 2008; Sakhalkar et al., 2007; Sharpe et al., 2002; Vinegoni et al., 2009; Walls et al., 2008; Zeng et al., 2015).

An alternative and complementary methods of whole-organ/body imaging can be performed with automated sectioning-imaging instruments (Osten and Margrie, 2013). The proposed setup allows users to skip the clearing step and yet obtain a high-resolution image without optic blurring throughout the sample. There are some possible drawbacks, however, when compared with clearing-imaging strategy. Because it requires physical sectioning time, throughput is lower compared to LSFM imaging. Tissue clearing also enables multi-scale (EM to macro-zoom imaging) and multi-modal (transgenes and chemical staining) data acquisition in a single sample, while the sectioning-imaging method destroys the sample in a single imaging sequence. A more complicated and expensive setup is also an obstacle to wider use for this type of instrument. However, these sectioning-imaging instruments have been utilized in several whole-organ imaging and data collection studies because of their advantages (Table S2). For example, serial two-photon (STP) tomography, a high-speed multi photon microscope with integrated vibratome sectioning (Ragan et al., 2012), has been used for RV-tracing, whole-brain *c-Fos* and *Arc* activity monitoring, and a large-scale mesoscopic connecome project with AAV tracing (Kim et al., 2015b; Oh et al., 2014; Velez-Fort et al., 2014; Vousden et al., 2015). Two-photon microscopy allows the user to take images of a deeper area from the sectioned surface and to obtain undisturbed optical sections. Another technique is micro-optical sectioning tomography (MOST) and the related instruments fluorescence-MOST (fMOST) and 2p-fMOST, which are composed of a microtome, a light microscope/scanning fluorescence microscope/two-photon microscope, and an image recorder (line-scan CCD or PMT) (Gong et al., 2013; Li et al., 2010; Wu et al., 2014; Zheng et al., 2013). Overall, the emerging sectioning and imaging techniques have already yielded interesting results, such as a brain-wide dataset at a high (~1 μm voxels) resolution, which is enough for reconstituting long-distance projections of individual axons in 3D space. In that case, the image collection took hundreds of hours for acquisition. Furthermore, a transparentized brain was also subjected to the STP tomography to exploit advantages of tissue clearing, which could expand its imaging depth (Costantini et al., 2015). As noted above, we do not think that a single method will offer a solution to all of the issues focused on by those who are interested in whole organ/body imaging applications; rather, we envision that finding creative ways to combine different methods, including those not yet developed, will provide greater opportunities.

Image Informatics for System Identification and System Analysis

One final aspect of whole-organ/body imaging at single-cell resolution that we want to highlight is how system-level biological information should be extracted from the acquired images. The omics-type approaches discussed here need processing of multi-dimensional data, including three dimensions with multi-color and -orientation images, and with multiple samples or timepoints. However, such large volumes of data, dozens of gigabytes to several terabytes for a single dataset, pose significant challenges for software and hardware and demand efficient solutions and have been often discussed in the scientific community (for example, see discussions in Akil et al., 2011). The informatics field for large image dataset analysis is in the early stage of development, facing challenges similar to those faced in the the first stage of the microarray era, because of insufficient software resources and hardware specs. Below we highlight some of the current efforts in this arena.

An example of the analysis pipeline is shown in Figure 5. Procedures following this general pipeline have been proposed and applied in several studies of multiple mammalian, fish, or fly datasets of whole-organ scale (Ahrens et al., 2013; Amat et al., 2015; Helmstaedter and Mitra, 2012; Menegas et al., 2015; Portugues et al., 2014; Susaki et al., 2014, 2015). Such pipelines can

Please cite this article as: Susaki and Ueda, Whole-body and Whole-Organ Clearing and Imaging Techniques with Single-Cell Resolution: Toward Organism-Level Systems Biology in Mammals, Cell Chemical Biology (2016), http://dx.doi.org/10.1016/j.chembiol.2015.11.009

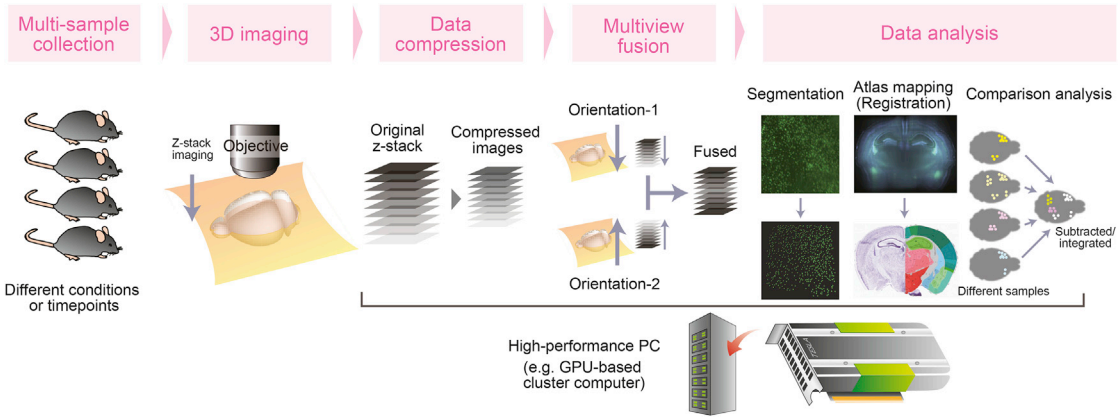

Figure 5. Possible Analysis Pipeline of Whole-Organ/Body Images

In the scheme of systems biology, multiple samples are generally prepared according to experimental conditions. Signals from labeled cells are comprehensively collected and subjected to the substantial analysis pipeline. In most cases, the acquired data are too big (gigabyte to terabyte, see Table S2) to be directly analyzed and thus should be compressed by changing file format and file size. If multi-orientation images are acquired for single specimens, they should be integrated to a single dataset for image complementation. This pre-processed data can then be used for various analyses to extract system-level biological information through structural segmentation, registration to atlas or between samples, and calculating differences among samples. These calculations are better supported by high-performance PC, such as GPU-based cluster computers. Three-dimensional brain data and reconstituted coronal section images were captured from the same dataset in Figure 4F. The brain atlas image was obtained from the Allen Institute for Brain Science, Allen Mouse Brain Atlas at http://mouse.brain-map.org (Lein et al., 2007).

be partly constructed by available software. In addition to commercially available software for 3D visualization and basic analysis (e.g., Imaris from Bitplane, Amira from FEI, Vision4D from arivis, and Image-Pro from MediaCybernetics), many open-source informatics tools for visualization and analysis have been developed, such as Fiji/ImageJ and its plugins (http://fiji.sc/Fiji); for example, BigDataViewer, http://fiji.sc/BigDataViewer (Pietzsch et al., 2015); CellProfiler, http://www.cellprofiler.org (Carpenter et al., 2006); KNOSSOS, http://www.knossostool.org (Helmstaedter et al., 2011); Vaa3D, http://home.penglab.com/proj/vaa3d/home/index.html (Peng et al., 2010); ITK-SNAP, http://www.itksnap.org/pmwiki/pmwiki.php (Yushkevich et al., 2006); Ssecrett and NeuroTrace, http://gvi.seas.harvard.edu/paper/ssecrett-and-neurotrace-interactive-visualization-and-analysis-tools-largescale-neuroscience-d (Jeong et al., 2010);OMERO, http://www.openmicroscopy.org/site/products/omero (Allan et al., 2012); goFigure2, http://gofigure2.sourceforge.net (Megason, 2009); CATMAID, http://catmaid.org/index.html (Saalfeld et al., 2009); ilastic, http://ilastik.org (Sommer et al., 2011); Icy, http://icy.bioimageanalysis.org (de Chaumont et al., 2012); BioImageXD, http://www.bioimagexd.net (Kankaanpaa et al., 2012); bioView3D, http://biodev.ece.ucsb.edu/webpages/software/bioView3D/ (Kvilekval et al., 2010); or VolView, http://www.kitware.com/opensource/volview.html (Kitware). In general, the experiments should be planned with care to balance the quality and quantity, because higher resolution images definitely increase the data size (Table S2). Furthermore, customized software and hardware solutions should be also considered for each experimental purpose in the current situation. For example, a high-spec hardware such as GPU-based cluster machines can accelerate the process, but issues in memory, algorism, data structure, processing, and storage should be simultaneously solved (Beyer et al., 2015).

In most cases, image size is reduced first to avoid overflow in hardware and calculation time. This is simply achieved by reducing image resolution and changing image format (Susaki et al., 2014, 2015). Although too much reduction causes loss of information, this can be avoided by the development of a proper lossless image format (e.g., Keller Lab Block or the KLB format that was recently reported in Amat et al., 2015) and software that can handle a larger data size.

If a single specimen is acquired as multiple image sets from different views or orientations, the image sets need to be merged again to a single dataset. Registration of different images is thus applied in this step and performed with ANTS software and nuclei counterstaining as a registration cue (Murphy et al., 2011; Susaki et al., 2014, 2015), with Amira software and autofluorescence image or manually selected landmark structures inside (Gong et al., 2013; Schwarz et al., 2015b), with Elastix software and an averaged autofluorescence shape (Klein et al., 2010; Menegas et al., 2015), with the Computational Morphometry Toolkit and summed stack images of time-lapse data (in the case of zebrafish larvae) (Portugues et al., 2014; Rohlfing and Maurer, 2003), or with an in-house image registration software and the averaged background shape (Vousden et al., 2015). The registration and alignment procedure have also been applied to further image analysis including atlas mapping or direct comparison analyses, as described below. Image fusion process could be performed by substantially calculating the degree of image sharpness and compensating the blurred part of the dataset with the shaper images acquired from different orientations (Susaki et al., 2014, 2015). In the other case, multi-view fusion was performed by introducing the assumption of determined acquisition directions (i.e., several orthogonal views) (Amat et al., 2015). This strategy is advantageous because it allows for throughput, scalability, and flexibility, while there are constraints in imaging setup and orientations. The fused dataset can be utilized for further image analysis, which possibly includes segmentation, quantification in atlas space, or direct comparison analysis.

 ©2016 Elsevier Ltd All rights reserved

Please cite this article as: Susaki and Ueda, Whole-body and Whole-Organ Clearing and Imaging Techniques with Single-Cell Resolution: Toward Organism-Level Systems Biology in Mammals, Cell Chemical Biology (2016), http://dx.doi.org/10.1016/j.chembiol.2015.11.009

Segmentation is a critical step for giving a biological meaning to the raw image data. Extraction of gross anatomical structures, like coronal vessels in the heart or the islets of Langerhans in the pancreas (Tainaka et al., 2014), or cellular to subcellular structureslike neurites or amyloid plaques (Chung et al., 2013; Costantini et al., 2015; Ertürk et al., 2012a, 2012b; Gong et al., 2013; Hama et al., 2011, 2015; Ke et al., 2013; Schwarz et al., 2015b; Soderblom et al., 2015) were tested in many studies. Furthermore, for the cellular resolution 3D images, segmentation of the cell body or the nuclei is most important and has been tried, for example, with 3D sphere approximation algorithms (Shimada et al., 2005; Quan et al., 2013, 2014), combination and expansion of 2D segmentation algorithms (Latorre et al., 2013), determination of cell centroids (Tsai et al., 2009; Wu et al., 2014), a combined approach of parametric contour evolution and spatiotemporal local data association rules (Amat et al., 2014), or even exploiting a machine-learning method in the process (Frasconi et al., 2014; Menegas et al., 2015; Silvestri et al., 2015) and a GPU machine workflow (Tracking with Gaussian Mixture Models software, or TGMM) (Amat et al., 2015). These segmentations also simplify the data contents to the essential pieces and further reduce the data size.

Registration is a critical step to map individual organ/body data to an atlas in order to compare multiple organ/body data samples in different conditions or time points. The registration to the well-annotated atlas also allows us to analyze organ/body data, e.g., count cells or quantify signal intensities, in a specific anatomical region by using annotation information associated with an atlas. In the neuroscience field, both 2D image- and 3D image-based brain atlas mapping were performed to reveal whole-brain neural circuitries or activities (Menegas et al., 2015; Oh et al., 2014; Pollak Dorocic et al., 2014; Schwarz et al., 2015b; Vousden et al., 2015; Zingg et al., 2014). For example, Menegas and colleagues recently reported a case of RV-based dopamine neuron circuit mapping with 77 brains out of eight injection sites. These brains were cleared and imaged with CLARITY and LSFM, registered across brains, and the labeled cell numbers extracted according to the anatomical space (Menegas et al., 2015).

Furthermore, to compare and integrate different experimental conditions or time points, direct alignment among samples was also performed. One example was in CUBIC studies that calculated signal subtraction of light-stimulated or unstimulated *Arc*-dVenus Tg mouse brains (Susaki et al., 2014, 2015). Not only the visual cortex, but several association regions were also identified as the stimulus-associated regions with cellular resolution. Faster timescale data of whole-brain functions were also examined in similar procedures; for example, Portugues et al. performed two-photon based time-lapse imaging of zebrafish larvae brains, expressing genetically encoded calcium indicator GCaMP5 (Portugues et al., 2014). Data from 13 brains were combined after registration and alignment, followed by the production of an averaged activity map and its dissection into functional networks. Such whole-brain functional imaging and data analysis in mammalian system appears too difficult in the current situation, but a combination of global snapshots of fixed brains with focused functional observations with faster timescale can be a possible substitute. An informatics tool for the functional brain mapping (both applicable for whole zebrafish brain and local mouse cortex) with cluster computing has also been proposed (Freeman et al., 2014).

All of these procedures contribute to identifying system components (i.e., the responsible cells) and analyzing their anatomical and functional connectivity from the large 3D or 4D imaging dataset, which will facilitate the systematic understanding of complex organism-level biological functions.

Concluding Remarks

As discussed here, comprehensive and quantitative experimental data in the cell-to-organism layers is now becoming available in mammalian studies. These technologies primarily help to comprehensively identify cellular circuits and quantitatively analyze their dynamics, which will lead to system-level understanding of the cellular circuits in the organisms. By using the technologies that we discussed here, the field can examine structure-dynamics relationships in the cellular circuits of interest at an increased depth that will eventually lead toward improved understanding of basic design principles. We think that this can be achieved if the strategies discussed here are combined with functional assays using perturbation tools and quantitative phenotyping or with temporal observations using assays in shorter timescales, such as fMRI, in vivo imaging, or electrophysiological experiments.

Along with their benefits for basic science, the systems-biological approaches in mammals have the potential to advance both the pharmaceutical and clinical fields. For example, high-throughput 3D imaging will provide an advanced drug screening approach by finding out the systematic responses throughout the body (Martinez et al., 2015). Three-dimensional analysis of clinical specimens will expand the ability to find pathological lesions and disease-related cells and will improve the sensitivity and objectivity of diagnosis and treatment. These are just some of the ways in which further improvements in whole-organ/body imaging are likely to have a positive impact on not only the life sciences, but the health sciences as well.

SUPPLEMENTAL INFORMATION

Supplemental Information includes References for Supplemental Tables and two tables and can be found with this article online at http://dx.doi.org/10.1016/j.chembiol.2015.11.009.

ACKNOWLEDGMENTS

We thank the people at The University of Tokyo, in particular T. Murakami, K. Tainaka, A. Kuno, M. Kaneko, T. Mano, T. Katsumata, K. Miyamichi, and T. Miyawaki for helping with manuscript and figure preparation. This work was supported by the Program for the Brain Mapping by Integrated Neurotechnologies for Disease Studies (Brain/MINDS) from the Ministry of Education, Culture, Sports, Science and Technology (MEXT) and AMED of Japan; by a Grant-in-Aid for Scientific Research (S) (25221004), a grant for Scientific Research on Innovative Areas (23115006) and for Young Scientists (A) (15H05650) from MEXT/Japan Society for the Promotion of Science (JSPS); by a grant from AMED-CREST and the Basic Science and Platform Technology Program for Innovative Biological Medicine from AMED; by PRESTO from JST; by the strategic programs for R&D (President's discretionary fund) of RIKEN; by an intramural Grant-in-Aid from the RIKEN QBiC; by a Grant-in-Aid from the Japan Foundation for Applied Enzymology; from the Brain Sciences Project of the Center for Novel Science Initiatives of the National Institutes of Natural Sciences (BS271005), and from the Tokyo Society of Medical Science. RIKEN has filed a provisional patent application based on the CUBIC works.

REFERENCES

Acar, M., Kocherlakota, K.S., Murphy, M.M., Peyer, J.G., Oguro, H., Inra, C.N., Jaiyeola, C., Zhao, Z., Luby-Phelps, K., and Morrison, S.J. (2015). Deep imaging of bone marrow shows non-dividing stem cells are mainly perisinusoidal. Nature *526*, 126–130.

Ahrens, M.B., Orger, M.B., Robson, D.N., Li, J.M., and Keller, P.J. (2013). Whole-brain functional imaging at cellular resolution using light-sheet microscopy. Nat. Methods *10*, 413–420.

Aida, T., Chiyo, K., Usami, T., Ishikubo, H., Imahashi, R., Wada, Y., Tanaka, K.F., Sakuma, T., Yamamoto, T., and Tanaka, K. (2015). Cloning-free CRISPR/Cas system facilitates functional cassette knock-in in mice. Genome Biol. *16*, 87.

Akil, H., Martone, M.E., and Van Essen, D.C. (2011). Challenges and opportunities in mining neuroscience data. Science *331*, 708–712.

Allan, C., Burel, J.M., Moore, J., Blackburn, C., Linkert, M., Loynton, S., Macdonald, D., Moore, W.J., Neves, C., Patterson, A., et al. (2012). OMERO: flexible, model-driven data management for experimental biology. Nat. Methods *9*, 245–253.

Alnuami, A.A., Zeedi, B., Qadri, S.M., and Ashraf, S.S. (2008). Oxyradical-induced GFP damage and loss of fluorescence. Int. J. Biol. Macromol. *43*, 182–186.

Amat, F., Lemon, W., Mossing, D.P., McDole, K., Wan, Y., Branson, K., Myers, E.W., and Keller, P.J. (2014). Fast, accurate reconstruction of cell lineages from large-scale fluorescence microscopy data. Nat. Methods *11*, 951–958.

Amat, F., Hockendorf, B., Wan, Y., Lemon, W.C., McDole, K., and Keller, P.J. (2015). Efficient processing and analysis of large-scale light-sheet microscopy data. Nat. Protoc. *10*, 1679–1696.

Anderson, G.A., Wong, M.D., Yang, J., and Henkelman, R.M. (2013). 3D imaging, registration, and analysis of the early mouse embryonic vasculature. Dev. Dyn. *242*, 527–538.

Aoyagi, Y., Kawakami, R., Osanai, H., Hibi, T., and Nemoto, T. (2015). A rapid optical clearing protocol using 2,2'-thiodiethanol for microscopic observation of fixed mouse brain. PLoS One *10*, e0116280.

Ascenzi, A., and Fabry, C. (1959). Technique for dissection and measurement of refractive index of osteones. J. Biophys. Biochem. Cytol. *6*, 139–142.

Barth, A.L., Gerkin, R.C., and Dean, K.L. (2004). Alteration of neuronal firing properties after *in vivo* experience in a FosGFP transgenic mouse. J. Neurosci. *24*, 6466–6475.

Baumgart, E., and Kubitscheck, U. (2012). Scanned light sheet microscopy with confocal slit detection. Opt. Express *20*, 21805–21814.

Beauvoit, B., Kitai, T., and Chance, B. (1994). Contribution of the mitochondrial compartment to the optical properties of the rat liver: a theoretical and practical approach. Biophys. J. *67*, 2501–2510.

Becker, K., Jährling, N., Saghafi, S., Weiler, R., and Dodt, H.U. (2012). Chemical clearing and dehydration of GFP expressing mouse brains. PLoS One *7*, e33916.

Begum, F., Zhu, W., Namaka, M.P., and Frost, E.E. (2010). A novel decalcification method for adult rodent bone for histological analysis of peripheral-central nervous system connections. J. Neurosci. Methods *187*, 59–66.

Belle, M., Godefroy, D., Dominici, C., Heitz-Marchaland, C., Zelina, P., Hellal, F., Bradke, F., and Chedotal, A. (2014). A simple method for 3D analysis of immunolabeled axonal tracts in a transparent nervous system. Cell Rep. *9*, 1191–1201.

Beuthan, J., Minet, O., Helfmann, J., Herrig, M., and Muller, G. (1996). The spatial variation of the refractive index in biological cells. Phys. Med. Biol. *41*, 369–382.

Beyer, J., Hadwiger, M., and Pfister, H. (2015). A survey of GPU-based large-scale volume visualization. Comput. Graph. Forum *34*, 1337.

Bolin, F.P., Preuss, L.E., Taylor, R.C., and Ference, R.J. (1989). Refractive-index of some mammalian-tissues using a fiber optic cladding method. Appl. Opt. *28*, 2297–2303.

Bria, A., and Iannello, G. (2012). TeraStitcher - a tool for fast automatic 3D-stitching of teravoxel-sized microscopy images. BMC Bioinformatics *13*, 316.

Buytaert, J.A., and Dirckx, J.J. (2007). Design and quantitative resolution measurements of an optical virtual sectioning three-dimensional imaging technique for biomedical specimens, featuring two-micrometer slicing resolution. J. Biomed. Opt. *12*, 014039.

Cai, D., Cohen, K.B., Luo, T., Lichtman, J.W., and Sanes, J.R. (2013). Improved tools for the Brainbow toolbox. Nat. Methods *10*, 540–547.

Callis, G., and Sterchi, D. (1998). Decalcification of bone: literature review and practical study of various decalcifying agents, methods, and their effects on bone histology. J. Histotechnol. *21*, 49–58.

Calve, S., Ready, A., Huppenbauer, C., Main, R., and Neu, C.P. (2015). Optical clearing in dense connective tissues to visualize cellular connectivity in situ. PLoS One *10*, e0116662.

Cancedda, L., Putignano, E., Impey, S., Maffei, L., Ratto, G.M., and Pizzorusso, T. (2003). Patterned vision causes CRE-mediated gene expression in the visual cortex through PKA and ERK. J. Neurosci. *23*, 7012–7020.

Carpenter, A.E., Jones, T.R., Lamprecht, M.R., Clarke, C., Kang, I.H., Friman, O., Guertin, D.A., Chang, J.H., Lindquist, R.A., Moffat, J., et al. (2006). CellProfiler: image analysis software for identifying and quantifying cell phenotypes. Genome Biol. *7*, R100.

Chance, B., Liu, H., Kitai, T., and Zhang, Y. (1995). Effects of solutes on optical properties of biological materials: models, cells, and tissues. Anal. Biochem. *227*, 351–362.

Chen, B.C., Legant, W.R., Wang, K., Shao, L., Milkie, D.E., Davidson, M.W., Janetopoulos, C., Wu, X.F.S., Hammer, J.A., Liu, Z., et al. (2014). Lattice light-sheet microscopy: imaging molecules to embryos at high spatiotemporal resolution. Science *346*, 1257998.

Chen, F., Tillberg, P.W., and Boyden, E.S. (2015). Expansion microscopy. Science *347*, 543–548.

Cheong, W.F., Prahl, S.A., and Welch, A.J. (1990). A review of the optical-properties of biological tissues. IEEE J. Quant. Electro. *26*, 2166–2185.

Chhetri, R.K., Amat, F., Wan, Y., Hockendorf, B., Lemon, W.C., and Keller, P.J. (2015). Whole-animal functional and developmental imaging with isotropic spatial resolution. Nat. Methods *12*, 1171–1178.

Chiang, A.-S. (October 2002). Aqueous Tissue Clearing Solution, U.S. patent 6472216 B1.

Choi, B., Tsu, L., Chen, E., Ishak, T.S., Iskandar, S.M., Chess, S., and Nelson, J.S. (2005). Determination of chemical agent optical clearing potential using in vitro human skin. Lasers Surg. Med. *36*, 72–75.

Chung, K., and Deisseroth, K. (2013). CLARITY for mapping the nervous system. Nat. Methods *10*, 508–513.

Chung, K., Wallace, J., Kim, S.Y., Kalyanasundaram, S., Andalman, A.S., Davidson, T.J., Mirzabekov, J.J., Zalocusky, K.A., Mattis, J., Denisin, A.K., et al. (2013). Structural and molecular interrogation of intact biological systems. Nature *497*, 332–337.

Cicchi, R., Sampson, D., Massi, D., and Pavone, F. (2005). Contrast and depth enhancement in two-photon microscopy of human skin ex vivo by use of optical clearing agents. Opt. Express *13*, 2337–2344.

Cifani, C., Koya, E., Navarre, B.M., Calu, D.J., Baumann, M.H., Marchant, N.J., Liu, Q.R., Khuc, T., Pickel, J., Lupica, C.R., et al. (2012). Medial prefrontal cortex neuronal activation and synaptic alterations after stress-induced reinstatement of palatable food seeking: a study using c-fos-GFP transgenic female rats. J. Neurosci. *32*, 8480–8490.

Cong, L., Ran, F.A., Cox, D., Lin, S., Barretto, R., Habib, N., Hsu, P.D., Wu, X., Jiang, W., Marraffini, L.A., et al. (2013). Multiplex genome engineering using CRISPR/Cas systems. Science *339*, 819–823.

Costantini, I., Ghobril, J.P., Di Giovanna, A.P., Mascaro, A.L., Silvestri, L., Mullenbroich, M.C., Onofri, L., Conti, V., Vanzi, F., Sacconi, L., et al. (2015). A versatile clearing agent for multi-modal brain imaging. Sci. Rep. *5*, 9808.

 ©2016 Elsevier Ltd All rights reserved

Davis, C.A., Holmyard, D.P., Millen, K.J., and Joyner, A.L. (1991). Examining pattern formation in mouse, chicken and frog embryos with an En-specific antiserum. Development *111*, 287–298.

de Chaumont, F., Dallongeville, S., Chenouard, N., Herve, N., Pop, S., Provoost, T., Meas-Yedid, V., Pankajakshan, P., Lecomte, T., Le Montagner, Y., et al. (2012). Icy: an open bioimage informatics platform for extended reproducible research. Nat. Methods *9*, 690–696.

Dean, K.M., and Fiolka, R. (2014). Uniform and scalable light-sheets generated by extended focusing. Opt. Express *22*, 26141–26152.

Denny, C.A., Kheirbek, M.A., Alba, E.L., Tanaka, K.F., Brachman, R.A., Laughman, K.B., Tomm, N.K., Turi, G.F., Losonczy, A., and Hen, R. (2014). Hippocampal memory traces are differentially modulated by experience, time, and adult neurogenesis. Neuron *83*, 189–201.

Dent, J.A., Polson, A.G., and Klymkowsky, M.W. (1989). A whole-mount immunocytochemical analysis of the expression of the intermediate filament protein vimentin in Xenopus. Development *105*, 61–74.

Deverman, B.E., and Patterson, P.H. (March 2015). Selective Recovery, U.S. patent 20150079038 A1.

Dodt, H.U., Leischner, U., Schierloh, A., Jährling, N., Mauch, C.P., Deininger, K., Deussing, J.M., Eder, M., Zieglgänsberger, W., and Becker, K. (2007). Ultramicroscopy: three-dimensional visualization of neuronal networks in the whole mouse brain. Nat. Methods *4*, 331–336.

Eguchi, M., and Yamaguchi, S. (2009). *In vivo* and *in vitro* visualization of gene expression dynamics over extensive areas of the brain. Neuroimage *44*, 1274–1283.

Emmenlauer, M., Ronneberger, O., Ponti, A., Schwarb, P., Griffa, A., Filippi, A., Nitschke, R., Driever, W., and Burkhardt, H. (2009). XuvTools: free, fast and reliable stitching of large 3D datasets. J. Microsc. *233*, 42–60.

Epp, J.R., Niibori, Y., Liz Hsiang, H.L., Mercaldo, V., Deisseroth, K., Josselyn, S.A., and Frankland, P.W. (2015). Optimization of CLARITY for clearing whole-brain and other intact organs (1,2,3). eNeuro *2*, http://dx.doi.org/10.1523/ENEURO.0022-15.2015.

Ertürk, A., Becker, K., Jährling, N., Mauch, C.P., Hojer, C.D., Egen, J.G., Hellal, F., Bradke, F., Sheng, M., and Dodt, H.U. (2012a). Three-dimensional imaging of solvent-cleared organs using 3DISCO. Nat. Protoc. *7*, 1983–1995.

Ertürk, A., Mauch, C.P., Hellal, F., Förstner, F., Keck, T., Becker, K., Jährling, N., Steffens, H., Richter, M., Hübener, M., et al. (2012b). Three-dimensional imaging of the unsectioned adult spinal cord to assess axon regeneration and glial responses after injury. Nat. Med. *18*, 166–171.

Ertürk, A., Lafkas, D., and Chalouni, C. (2014). Imaging cleared intact biological systems at a cellular level by 3DISCO. J. Vis. Exp. *89*, e51382.

Fagan, J.M., Sleczka, B.G., and Sohar, I. (1999). Quantitation of oxidative damage to tissue proteins. Int. J. Biochem. Cell Biol. *31*, 751–757.

Fahrbach, F.O., and Rohrbach, A. (2012). Propagation stability of self-reconstructing Bessel beams enables contrast-enhanced imaging in thick media. Nat. Commun. *3*, 632.

Fahrbach, F.O., Simon, P., and Rohrbach, A. (2010). Microscopy with self-reconstructing beams. Nat. Photon. *4*, 780–785.

Frasconi, P., Silvestri, L., Soda, P., Cortini, R., Pavone, F.S., and Iannello, G. (2014). Large-scale automated identification of mouse brain cells in confocal light sheet microscopy images. Bioinformatics *30*, i587–593.

Freeman, J., Vladimirov, N., Kawashima, T., Mu, Y., Sofroniew, N.J., Bennett, D.V., Rosen, J., Yang, C.T., Looger, L.L., and Ahrens, M.B. (2014). Mapping brain activity at scale with cluster computing. Nat. Methods *11*, 941–950.

Friedrich, M., Gan, Q., Ermolayev, V., and Harms, G.S. (2011). STED-SPIM: stimulated emission depletion improves sheet illumination microscopy resolution. Biophys. J. *100*, L43–L45.

Genina, E.A., Bashkatov, A.N., and Tuchin, V.V. (2008). Optical clearing of cranial bone. Adv. Opt. Tech.. http://dx.doi.org/10.1155/2008/267867

Gerfen, C.R., Paletzki, R., and Heintz, N. (2013). GENSAT BAC Cre-recombinase driver lines to study the functional organization of cerebral cortical and basal ganglia circuits. Neuron *80*, 1368–1383.

Gleave, J.A., Wong, M.D., Dazai, J., Altaf, M., Henkelman, R.M., Lerch, J.P., and Nieman, B.J. (2012). Neuroanatomical phenotyping of the mouse brain with three-dimensional autofluorescence imaging. Physiol. Genomics *44*, 778–785.

Gleave, J.A., Lerch, J.P., Henkelman, R.M., and Nieman, B.J. (2013). A method for 3D immunostaining and optical imaging of the mouse brain demonstrated in neural progenitor cells. PLoS One *8*, e72039.

Gomes, S.A., dos Reis, L.M., de Oliveira, I.B., Noronha, I.D.L., Jorgetti, V., and Heilberg, I.P. (2008). Usefulness of a quick decalcification of bone sections embedded in methyl metacrylate: an improved method for immunohistochemistry. J. Bone Miner. Metab. *26*, 110–113.

Gong, S.C., Doughty, M., Harbaugh, C.R., Cummins, A., Hatten, M.E., Heintz, N., and Gerfen, C.R. (2007). Targeting Cre recombinase to specific neuron populations with bacterial artificial chromosome constructs. J. Neurosci. *27*, 9817–9823.

Gong, H., Zeng, S.Q., Yan, C., Lv, X.H., Yang, Z.Q., Xu, T.H., Feng, Z., Ding, W.X., Qi, X.L., Li, A.A., et al. (2013). Continuously tracing brain-wide long-distance axonal projections in mice at a one-micron voxel resolution. Neuroimage *74*, 87–98.

Grinevich, V., Kolleker, A., Eliava, M., Takada, N., Takuma, H., Fukazawa, Y., Shigemoto, R., Kuhl, D., Waters, J., Seeburg, P.H., et al. (2009). Fluorescent Arc/Arg3.1 indicator mice: a versatile tool to study brain activity changes in vitro and in vivo. J. Neurosci. Methods *184*, 25–36.

Guenthner, C.J., Miyamichi, K., Yang, H.H., Heller, H.C., and Luo, L. (2013). Permanent genetic access to transiently active neurons via TRAP: targeted recombination in active populations. Neuron *78*, 773–784.

Hama, H., Kurokawa, H., Kawano, H., Ando, R., Shimogori, T., Noda, H., Fukami, K., Sakaue-Sawano, A., and Miyawaki, A. (2011). Sca*l*e: a chemical approach for fluorescence imaging and reconstruction of transparent mouse brain. Nat. Neurosci. *14*, 1481–1488.

Hama, H., Hioki, H., Namiki, K., Hoshida, T., Kurokawa, H., Ishidate, F., Kaneko, T., Akagi, T., Saito, T., Saido, T., et al. (2015). ScaleS: an optical clearing palette for biological imaging. Nat. Neurosci. *18*, 1518–1529.

Haupts, U., Maiti, S., Schwille, P., and Webb, W.W. (1998). Dynamics of fluorescence fluctuations in green fluorescent protein observed by fluorescence correlation spectroscopy. Proc. Natl. Acad. Sci. USA *95*, 13573–13578.

Helmchen, F., and Denk, W. (2005). Deep tissue two-photon microscopy. Nat. Methods *2*, 932–940.

Helmstaedter, M., and Mitra, P.P. (2012). Computational methods and challenges for large-scale circuit mapping. Curr. Opin. Neurobiol. *22*, 162–169.

Helmstaedter, M., Briggman, K.L., and Denk, W. (2011). High-accuracy neurite reconstruction for high-throughput neuroanatomy. Nat. Neurosci. *14*, 1081–1088.

Higashiyama, H., Sumitomo, H., Ozawa, A., Igarashi, H., Tsunekawa, N., Kurohmaru, M., and Kanai, Y. (2015). Anatomy of the murine hepatobiliary system: a whole-organ-level analysis using a transparency method. Anat. Rec. (Hoboken). http://dx.doi.org/10.1002/ar.23287.

Hirashima, T., and Adachi, T. (2015). Procedures for the quantification of whole-tissue immunofluorescence images obtained at single-cell resolution during murine tubular organ development. PLoS One *10*, e0135343.

Horecker, B.L. (1943). The absorption spectra of hemoglobin and its derivatives in the visible and near infra-red regions. J. Biol. Chem. *148*, 173–183.

Hou, B., Zhang, D., Zhao, S., Wei, M., Yang, Z., Wang, S., Wang, J., Zhang, X., Liu, B., Fan, L., et al. (2015). Scalable and Dil-compatible optical clearance of the mammalian brain. Front. Neuroanat. *9*, 19.

Huang, Z.J., and Zeng, H. (2013). Genetic approaches to neural circuits in the mouse. Annu. Rev. Neurosci. *36*, 183–215.

Jeansson, M., Gawlik, A., Anderson, G., Li, C., Kerjaschki, D., Henkelman, M., and Quaggin, S.E. (2011). Angiopoietin-1 is essential in mouse vasculature during development and in response to injury. J. Clin. Invest *121*, 2278–2289.

Jeong, W.K., Beyer, J., Hadwiger, M., Blue, R., Law, C., Vazquez-Reina, A., Reid, R.C., Lichtman, J., and Pfister, H. (2010). Ssecrett and NeuroTrace: interactive visualization and analysis tools for large-scale neuroscience data sets. IEEE Comput. Graph. Appl. *30*, 58–70.

Jiang, J., and Wang, R.K. (2004). Comparing the synergistic effects of oleic acid and dimethyl sulfoxide as vehicles for optical clearing of skin tissue in vitro. Phys. Med. Biol. *49*, 5283–5294.

Johnsen, S., and Widder, E.A. (1999). The physical basis of transparency in biological tissue: ultrastructure and the minimization of light scattering. J. Theor. Biol. *199*, 181–198.

Kalchmair, S., Jahrling, N., Becker, K., and Dodt, H.U. (2010). Image contrast enhancement in confocal ultramicroscopy. Opt. Lett. *35*, 79–81.

Kankaanpaa, P., Paavolainen, L., Tiitta, S., Karjalainen, M., Paivarinne, J., Nieminen, J., Marjomaki, V., Heino, J., and White, D.J. (2012). BioImageXD: an open, general-purpose and high-throughput image-processing platform. Nat. Methods *9*, 683–689.

Kawashima, T., Okuno, H., Nonaka, M., Adachi-Morishima, A., Kyo, N., Okamura, M., Takemoto-Kimura, S., Worley, P.F., and Bito, H. (2009). Synaptic activity-responsive element in the Arc/Arg3.1 promoter essential for synapse-to-nucleus signaling in activated neurons. Proc. Natl. Acad. Sci. USA *106*, 316–321.

Kawashima, T., Kitamura, K., Suzuki, K., Nonaka, M., Kamijo, S., Takemoto-Kimura, S., Kano, M., Okuno, H., Ohki, K., and Bito, H. (2013). Functional labeling of neurons and their projections using the synthetic activity–dependent promoter E-SARE. Nat. Methods *10*, 889–895.

Kawashima, T., Okuno, H., and Bito, H. (2014). A new era for functional labeling of neurons: activity-dependent promoters have come of age. Front. Neural Circuits *8*, 37.

Ke, M.T., Fujimoto, S., and Imai, T. (2013). SeeDB: a simple and morphology-preserving optical clearing agent for neuronal circuit reconstruction. Nat. Neurosci. *16*, 1154–1161.

Keller, P.J., and Ahrens, M.B. (2015). Visualizing whole-brain activity and development at the single-cell level using light-sheet microscopy. Neuron *85*, 462–483.

Keller, P.J., and Dodt, H.U. (2012). Light sheet microscopy of living or cleared specimens. Curr. Opin. Neurobiol. *22*, 138–143.

Keller, P.J., Schmidt, A.D., Wittbrodt, J., and Stelzer, E.H.K. (2008). Reconstruction of zebrafish early embryonic development by scanned light sheet microscopy. Science *322*, 1065–1069.

Keller, P.J., Schmidt, A.D., Santella, A., Khairy, K., Bao, Z.R., Wittbrodt, J., and Stelzer, E.H.K. (2010). Fast, high-contrast imaging of animal development with scanned light sheet-based structured-illumination microscopy. Nat. Methods *7*, 637–642.

Kim, J., Zhao, T., Petralia, R.S., Yu, Y., Peng, H., Myers, E., and Magee, J.C. (2012). mGRASP enables mapping mammalian synaptic connectivity with light microscopy. Nat. Methods *9*, 96–102.

Kim, S.Y., Cho, J.H., Murray, E., Bakh, N., Choi, H., Ohn, K., Ruelas, L., Hubbert, A., McCue, M., Vassallo, S.L., et al. (2015a). Stochastic electrotransport selectively enhances the transport of highly electromobile molecules. Proc. Natl. Acad. Sci. USA *112*, E6274–E6283.

Kim, Y., Venkataraju, K.U., Pradhan, K., Mende, C., Taranda, J., Turaga, S.C., Arganda-Carreras, I., Ng, L., Hawrylycz, M.J., Rockland, K.S., et al. (2015b). Mapping social behavior-induced brain activation at cellular resolution in the mouse. Cell Rep. *10*, 292–305.

Kitano, H. (2002). Systems biology: a brief overview. Science *295*, 1662–1664.

Kiyonari, H., Kaneko, M., Abe, S., and Aizawa, S. (2010). Three inhibitors of FGF receptor, ERK, and GSK3 establishes germline-competent embryonic stem cells of C57BL/6N mouse strain with high efficiency and stability. Genesis *48*, 317–327.

Klein, S., Staring, M., Murphy, K., Viergever, M.A., and Pluim, J.P. (2010). elastix: a toolbox for intensity-based medical image registration. IEEE Trans. Med. Imaging *29*, 196–205.

Kristinsson, H.G., and Hultin, H.O. (2004). Changes in trout hemoglobin conformations and solubility after exposure to acid and alkali pH. J. Agric. Food Chem. *52*, 3633–3643.

Krzic, U., Gunther, S., Saunders, T.E., Streichan, S.J., and Hufnagel, L. (2012). Multiview light-sheet microscope for rapid in toto imaging. Nat. Methods *9*, 730–733.

Kurihara, D., Mizuta, Y., Sato, Y., and Higashiyama, T. (2015). ClearSee: a rapid optical clearing reagent for whole-plant fluorescence imaging. Development *142*, 4168–4179.

Kuwajima, T., Sitko, A.A., Bhansali, P., Jurgens, C., Guido, W., and Mason, C. (2013). *Clear*^{T}: a detergent- and solvent-free clearing method for neuronal and non-neuronal tissue. Development *140*, 1364–1368.

Kvilekval, K., Fedorov, D., Obara, B., Singh, A., and Manjunath, B.S. (2010). Bisque: a platform for bioimage analysis and management. Bioinformatics *26*, 544–552.

Latorre, A., Alonso-Nanclares, L., Muelas, S., Pena, J.M., and Defelipe, J. (2013). 3D segmentations of neuronal nuclei from confocal microscope image stacks. Front. Neuroanat. *7*, 49.

Lee, H., Park, J.H., Seo, I., Park, S.H., and Kim, S. (2014). Improved application of the electrophoretic tissue clearing technology, CLARITY, to intact solid organs including brain, pancreas, liver, kidney, lung, and intestine. BMC Dev. Biol. *14*, 48.

Lein, E.S., Hawrylycz, M.J., Ao, N., Ayres, M., Bensinger, A., Bernard, A., Boe, A.F., Boguski, M.S., Brockway, K.S., Byrnes, E.J., et al. (2007). Genome-wide atlas of gene expression in the adult mouse brain. Nature *445*, 168–176.

Leischner, U., Zieglgansberger, W., and Dodt, H.U. (2009). Resolution of ultramicroscopy and field of view analysis. PLoS One *4*, e5785.

Lemon, W.C., Pulver, S.R., Hockendorf, B., McDole, K., Branson, K., Freeman, J., and Keller, P.J. (2015). Whole-central nervous system functional imaging in larval Drosophila. Nat. Commun. *6*, 7924.

Lerner, T.N., Shilyansky, C., Davidson, T.J., Evans, K.E., Beier, K.T., Zalocusky, K.A., Crow, A.K., Malenka, R.C., Luo, L., Tomer, R., et al. (2015). Intact-brain analyses reveal distinct information carried by SNc dopamine subcircuits. Cell *162*, 635–647.

Li, A.A., Gong, H., Zhang, B., Wang, Q.D., Yan, C., Wu, J.P., Liu, Q.A., Zeng, S.Q., and Luo, Q.M. (2010). Micro-optical sectioning tomography to obtain a high-resolution atlas of the mouse brain. Science *330*, 1404–1408.

Li, J., Czajkowsky, D.M., Li, X., and Shao, Z. (2015). Fast immuno-labeling by electrophoretically driven infiltration for intact tissue imaging. Sci. Rep. *5*, 10640.

Liu, H., Beauvoit, B., Kimura, M., and Chance, B. (1996). Dependence of tissue optical properties on solute-induced changes in refractive index and osmolarity. J. Biomed. Opt. *1*, 200–211.

Livet, J., Weissman, T.A., Kang, H., Draft, R.W., Lu, J., Bennis, R.A., Sanes, J.R., and Lichtman, J.W. (2007). Transgenic strategies for combinatorial expression of fluorescent proteins in the nervous system. Nature *450*, 56–62.

Luo, L., Callaway, E.M., and Svoboda, K. (2008). Genetic dissection of neural circuits. Neuron *57*, 634–660.

Luque, J.M., Adams, W.B., and Nicholls, J.G. (1998a). Procedures for whole-mount immunohistochemistry and in situ hybridization of immature mammalian CNS. Brain Res. Brain Res. Protoc. *2*, 165–173.

Luque, J.M., Biou, V., and Nicholls, J.G. (1998b). Three-dimensional visualization of the distribution, growth, and regeneration of monoaminergic neurons in whole mounts of immature mammalian CNS. J. Comp. Neurol. *390*, 427–438.

Madisen, L., Zwingman, T.A., Sunkin, S.M., Oh, S.W., Zariwala, H.A., Gu, H., Ng, L.L., Palmiter, R.D., Hawrylycz, M.J., Jones, A.R., et al. (2010). A robust and high-throughput Cre reporting and characterization system for the whole mouse brain. Nat. Neurosci. *13*, 133–140.

Mao, Z., Zhu, D., Hu, Y., Wen, X., and Han, Z. (2008). Influence of alcohols on the optical clearing effect of skin in vitro. J. Biomed. Opt. *13*, 021104.

Martinez, N.J., Titus, S.A., Wagner, A.K., and Simeonov, A. (2015). High-throughput fluorescence imaging approaches for drug discovery using in vitro and in vivo three-dimensional models. Expert Opin. Drug Discov. *10*, 1347–1361.

McGurk, L., Morrison, H., Keegan, L.P., Sharpe, J., and O'Connell, M.A. (2007). Three-dimensional imaging of Drosophila melanogaster. PLoS One *2*, e834.

Megason, S.G. (2009). In toto imaging of embryogenesis with confocal time-lapse microscopy. Methods Mol. Biol. *546*, 317–332.

 ©2016 Elsevier Ltd All rights reserved

Menegas, W., Bergan, J.F., Ogawa, S.K., Isogai, Y., Umadevi Venkataraju, K., Osten, P., Uchida, N., and Watabe-Uchida, M. (2015). Dopamine neurons projecting to the posterior striatum form an anatomically distinct subclass. Elife *4*, e10032.

Meyer, R.A. (1979). Light scattering from biological cells: dependence of backscatter radiation on membrane thickness and refractive index. Appl. Opt. *18*, 585–588.

Mikula, S., and Denk, W. (2015). High-resolution whole-brain staining for electron microscopic circuit reconstruction. Nat. Methods *12*, 541–546.

Miyawaki, A. (2015). Brain clearing for connectomics. Microscopy (Oxf.) *64*, 5–8.

Mourant, J.R., Freyer, J.P., Hielscher, A.H., Eick, A.A., Shen, D., and Johnson, T.M. (1998). Mechanisms of light scattering from biological cells relevant to noninvasive optical-tissue diagnostics. Appl. Opt. *37*, 3586–3593.

Murphy, K., van Ginneken, B., Reinhardt, J.M., Kabus, S., Ding, K., Deng, X., Cao, K., Du, K., Christensen, G.E., Garcia, V., et al. (2011). Evaluation of registration methods on thoracic CT: the EMPIRE10 challenge. IEEE Trans. Med. Imaging *30*, 1901–1920.

Niedworok, C.J., Schwarz, I., Ledderose, J., Giese, G., Conzelmann, K.K., and Schwarz, M.K. (2012). Charting monosynaptic connectivity maps by two-color light-sheet fluorescence microscopy. Cell Rep. *2*, 1375–1386.

Ode, K.L., and Ueda, H.R. (2015). Seeing the forest and trees: whole-body and whole-brain imaging for circadian biology. Diabetes Obes. Metab. *17* (*Suppl 1*), 47–54.

Oh, S.W., Harris, J.A., Ng, L., Winslow, B., Cain, N., Mihalas, S., Wang, Q., Lau, C., Kuan, L., Henry, A.M., et al. (2014). A mesoscale connectome of the mouse brain. Nature *508*, 207–214.

Ohmi, M., Ohnishi, Y., Yoden, K., and Haruna, M. (2000). In vitro simultaneous measurement of refractive index and thickness of biological tissue by the low coherence interferometry. IEEE Trans. Biomed. Eng. *47*, 1266–1270.

Oldham, M., Sakhalkar, H., Oliver, T., Allan Johnson, G., and Dewhirst, M. (2008). Optical clearing of unsectioned specimens for three-dimensional imaging via optical transmission and emission tomography. J. Biomed. Opt. *13*, 021113.

Oliver, C.N., Ahn, B.W., Moerman, E.J., Goldstein, S., and Stadtman, E.R. (1987). Age-related changes in oxidized proteins. J. Biol. Chem. *262*, 5488–5491.

Osakada, F., and Callaway, E.M. (2013). Design and generation of recombinant rabies virus vectors. Nat. Protoc. *8*, 1583–1601.

Osten, P., and Margrie, T.W. (2013). Mapping brain circuitry with a light microscope. Nat. Methods *10*, 515–523.

Panier, T., Romano, S.A., Olive, R., Pietri, T., Sumbre, G., Candelier, R., and Debregeas, G. (2013). Fast functional imaging of multiple brain regions in intact zebrafish larvae using selective plane illumination microscopy. Front. Neural Circuits *7*, 65.

Peng, H., Ruan, Z., Long, F., Simpson, J.H., and Myers, E.W. (2010). V3D enables real-time 3D visualization and quantitative analysis of large-scale biological image data sets. Nat. Biotechnol. *28*, 348–353.

Pietzsch, T., Saalfeld, S., Preibisch, S., and Tomancak, P. (2015). BigDataViewer: visualization and processing for large image data sets. Nat. Methods *12*, 481–483.

Planchon, T.A., Gao, L., Milkie, D.E., Davidson, M.W., Galbraith, J.A., Galbraith, C.G., and Betzig, E. (2011). Rapid three-dimensional isotropic imaging of living cells using Bessel beam plane illumination. Nat. Methods *8*, 417–423.

Pollak Dorocic, I., Furth, D., Xuan, Y., Johansson, Y., Pozzi, L., Silberberg, G., Carlen, M., and Meletis, K. (2014). A whole-brain atlas of inputs to serotonergic neurons of the dorsal and median raphe nuclei. Neuron *83*, 663–678.

Portugues, R., Feierstein, C.E., Engert, F., and Orger, M.B. (2014). Whole-brain activity maps reveal stereotyped, distributed networks for visuomotor behavior. Neuron *81*, 1328–1343.

Potsch, L., Skopp, G., and Rippin, G. (1997). A comparison of 3H-cocaine binding on melanin granules and human hair in vitro. Int. J. Leg. Med. *110*, 55–62.

Poueymirou, W.T., Auerbach, W., Frendewey, D., Hickey, J.F., Escaravage, J.M., Esau, L., Dore, A.T., Stevens, S., Adams, N.C., Dominguez, M.G., et al. (2007). F0 generation mice fully derived from gene-targeted embryonic stem cells allowing immediate phenotypic analyses. Nat. Biotechnol. *25*, 91–99.

Quan, T., Zheng, T., Yang, Z., Ding, W., Li, S., Li, J., Zhou, H., Luo, Q., Gong, H., and Zeng, S. (2013). NeuroGPS: automated localization of neurons for brain circuits using L1 minimization model. Sci. Rep. *3*, 1414.

Quan, T., Li, J., Zhou, H., Li, S., Zheng, T., Yang, Z., Luo, Q., Gong, H., and Zeng, S. (2014). Digital reconstruction of the cell body in dense neural circuits using a spherical-coordinated variational model. Sci. Rep. *4*, 4970.

Quinta, H.R., Pasquini, L.A., and Pasquini, J.M. (2015). Three-dimensional reconstruction of corticospinal tract using one-photon confocal microscopy acquisition allows detection of axonal disruption in spinal cord injury. J. Neurochem. *133*, 113–124.

Ragan, T., Kadiri, L.R., Venkataraju, K.U., Bahlmann, K., Sutin, J., Taranda, J., Arganda-Carreras, I., Kim, Y., Seung, H.S., and Osten, P. (2012). Serial two-photon tomography for automated ex vivo mouse brain imaging. Nat. Methods *9*, 255–258.

Randlett, O.W., Wee, C.L., Naumann, E.A., Onyeka Nnaemeka, O., Schoppik, D., Fitzgerald, J.E., Portugues, R., Lacoste, A.M.B., Riegler, C., Engert, F., and Schier, A.F. (2015). Whole-brain activity mapping onto a zebrafish brain atlas. Nat. Methods *12*, 1039–1046.

Reijmers, L.G., Perkins, B.L., Matsuo, N., and Mayford, M. (2007). Localization of a stable neural correlate of associative memory. Science *317*, 1230–1233.

Renier, N., Wu, Z., Simon, D.J., Yang, J., Ariel, P., and Tessier-Lavigne, M. (2014). iDISCO: a simple, rapid method to immunolabel large tissue samples for volume imaging. Cell *159*, 896–910.

Richardson, D.S., and Lichtman, J.W. (2015). Clarifying tissue clearing. Cell *162*, 246–257.

Rohlfing, T., and Maurer, C.R., Jr. (2003). Nonrigid image registration in shared-memory multiprocessor environments with application to brains, breasts, and bees. IEEE Trans. Inf. Technol. Biomed. *7*, 16–25.

Rylander, C.G., Stumpp, O.F., Milner, T.E., Kemp, N.J., Mendenhall, J.M., Diller, K.R., and Welch, A.J. (2006). Dehydration mechanism of optical clearing in tissue. J. Biomed. Opt. *11*, 041117.

Saalfeld, S., Cardona, A., Hartenstein, V., and Tomancak, P. (2009). CATMAID: collaborative annotation toolkit for massive amounts of image data. Bioinformatics *25*, 1984–1986.

Sakhalkar, H.S., Dewhirst, M., Oliver, T., Cao, Y., and Oldham, M. (2007). Functional imaging in bulk tissue specimens using optical emission tomography: fluorescence preservation during optical clearing. Phys. Med. Biol. *52*, 2035–2054.

Santi, P.A., Johnson, S.B., Hillenbrand, M., GrandPre, P.Z., Glass, T.J., and Leger, J.R. (2009). Thin-sheet laser imaging microscopy for optical sectioning of thick tissues. Biotechniques *46*, 287–294.

Schilling, K., Luk, D., Morgan, J.I., and Curran, T. (1991). Regulation of a fos-lacZ fusion gene: a paradigm for quantitative analysis of stimulus-transcription coupling. Proc. Natl. Acad. Sci. USA *88*, 5665–5669.

Schwarz, L.A., Miyamichi, K., Gao, X.J., Beier, K.T., Weissbourd, B., DeLoach, K.E., Ren, J., Ibanes, S., Malenka, R.C., Kremer, E.J., et al. (2015a). Viral-genetic tracing of the input-output organization of a central noradrenaline circuit. Nature *524*, 88–92.

Schwarz, M.K., Scherbarth, A., Sprengel, R., Engelhardt, J., Theer, P., and Giese, G. (2015b). Fluorescent-protein stabilization and high-resolution imaging of cleared, intact mouse brains. PLoS One *10*, e0124650.

Sharpe, J., Ahlgren, U., Perry, P., Hill, B., Ross, A., Hecksher-Sorensen, J., Baldock, R., and Davidson, D. (2002). Optical projection tomography as a tool for 3D microscopy and gene expression studies. Science *296*, 541–545.

Shimada, T., Kato, K., Kamikouchi, A., and Ito, K. (2005). Analysis of the distribution of the brain cells of the fruit fly by an automatic cell counting algorithm. Physica A Stat. Mech. Appl. *350*, 144–149.

Siedentopf, H., and Zsigmondy, R. (1903). Über Sichtbarmachung und Größenbestimmung ultramikroskopischer Teilchen, mit besonderer Anwendung auf Goldrubingläser. Ann. Phys. *315*, 1–39.

Please cite this article as: Susaki and Ueda, Whole-body and Whole-Organ Clearing and Imaging Techniques with Single-Cell Resolution: Toward Organism-Level Systems Biology in Mammals, Cell Chemical Biology (2016), http://dx.doi.org/10.1016/j.chembiol.2015.11.009

Sillitoe, R.V., and Hawkes, R. (2002). Whole-mount immunohistochemistry: a high-throughput screen for patterning defects in the mouse cerebellum. J. Histochem. Cytochem. *50*, 235–244.

Silvestri, L., Bria, A., Sacconi, L., Iannello, G., and Pavone, F.S. (2012). Confocal light sheet microscopy: micron-scale neuroanatomy of the entire mouse brain. Opt. Express *20*, 20582–20598.

Silvestri, L., Paciscopi, M., Soda, P., Biamonte, F., Iannello, G., Frasconi, P., and Pavone, F.S. (2015). Quantitative neuroanatomy of all Purkinje cells with light sheet microscopy and high-throughput image analysis. Front. Neuroanat. *9*, 68.

Smeyne, R.J., Schilling, K., Robertson, L., Luk, D., Oberdick, J., Curran, T., and Morgan, J.I. (1992). fos-lacZ transgenic mice: mapping sites of gene induction in the central nervous system. Neuron *8*, 13–23.

Soderblom, C., Lee, D.H., Dawood, A., Carballosa, M., Jimena Santamaria, A., Benavides, F.D., Jergova, S., Grumbles, R.M., Thomas, C.K., Park, K.K., et al. (2015). 3D imaging of axons in transparent spinal cords from rodents and nonhuman primates. eNeuro *2*, e0001–0015.

Sommer, C., Straehle, C., Kothe, U., and Hamprecht, F.A. (2011). Ilastik: Interactive learning and segmentation toolkit. Proc. 8th IEEE Int. Symp. Biomed. Imag, 230–233.

Spalteholz, W. (1914). Über das Durchsichtigmachen von menschlichen und tierischen Präparaten (S. Hirzel, Leipzig).

Staudt, T., Lang, M.C., Medda, R., Engelhardt, J., and Hell, S.W. (2007). 2,2'-Thiodiethanol: a new water soluble mounting medium for high resolution optical microscopy. Microsc. Res. Tech. *70*, 1–9.

Steinke, J.M., and Shepherd, A.P. (1988). Comparison of Mie theory and the light scattering of red blood cells. Appl. Opt. *27*, 4027–4033.

Steinke, H., and Wolff, W. (2001). A modified Spalteholz technique with preservation of the histology. Ann. Anat. *183*, 91–95.

Susaki, E.A., Tainaka, K., Perrin, D., Kishino, F., Tawara, T., Watanabe, T.M., Yokoyama, C., Onoe, H., Eguchi, M., Yamaguchi, S., et al. (2014). Whole-brain imaging with single-cell resolution using chemical cocktails and computational analysis. Cell *157*, 726–739.

Susaki, E.A., Tainaka, K., Perrin, D., Yukinaga, H., Kuno, A., and Ueda, H.R. (2015). Advanced CUBIC protocols for whole-brain and whole-body clearing and imaging. Nat. Protoc. *10*, 1709–1727.

Tainaka, K., Kubota, S.I., Suyama, T.Q., Susaki, E.A., Perrin, D., Ukai-Tadenuma, M., Ukai, H., and Ueda, H.R. (2014). Whole-body imaging with single-cell resolution by tissue decolorization. Cell *159*, 911–924.

Tomer, R., Khairy, K., Amat, F., and Keller, P.J. (2012). Quantitative high-speed imaging of entire developing embryos with simultaneous multiview light-sheet microscopy. Nat. Methods *9*, 755–763.

Tomer, R., Ye, L., Hsueh, B., and Deisseroth, K. (2014). Advanced CLARITY for rapid and high-resolution imaging of intact tissues. Nat. Protoc. *9*, 1682–1697.

Treweek, J.B., Chan, K.Y., Flytzanis, N.C., Yang, B., Deverman, B.E., Greenbaum, A., Lignell, A., Xiao, C., Cai, L., Ladinsky, M.S., et al. (2015). Whole-body tissue stabilization and selective extractions via tissue-hydrogel hybrids for high-resolution intact circuit mapping and phenotyping. Nat. Protoc. *10*, 1860–1896.

Truong, T.V., Supatto, W., Koos, D.S., Choi, J.M., and Fraser, S.E. (2011). Deep and fast live imaging with two-photon scanned light-sheet microscopy. Nat. Methods *8*, 757–760.

Tsai, P.S., Kaufhold, J.P., Blinder, P., Friedman, B., Drew, P.J., Karten, H.J., Lyden, P.D., and Kleinfeld, D. (2009). Correlations of neuronal and microvascular densities in murine cortex revealed by direct counting and colocalization of nuclei and vessels. J. Neurosci. *29*, 14553–14570.

Tuchin, V.V. (2015). Tissue optics and photonics: light-tissue interaction. J. Biomed. Photon. Eng. *1*, 98–134.

Tuchin, V.V., Maksimova, I.L., Zimnyakov, D.A., Kon, I.L., Mavlyutov, A.H., and Mishin, A.A. (1997). Light propagation in tissues with controlled optical properties. J. Biomed. Opt. *2*, 401–417.

Turaga, D., and Holy, T.E. (2010). Image-based calibration of a deformable mirror in wide-field microscopy. Appl. Opt. *49*, 2030–2040.

Unnersjö-Jess, D., Scott, L., Blom, H., and Brismar, H. (2015). Super-resolution stimulated emission depletion imaging of slit diaphragm proteins in optically cleared kidney tissue. Kidney Int. http://dx.doi.org/10.1038/ki.2015.308.

van Staveren, H.J., Moes, C.J., van Marie, J., Prahl, S.A., and van Gemert, M.J. (1991). Light scattering in Intralipid-10% in the wavelength range of 400-1100 nm. Appl. Opt. *30*, 4507–4514.

Vargas, O., Chan, E.K., Barton, J.K., Rylander, H.G., and Welch, A.J. (1999). Use of an agent to reduce scattering in skin. Lasers Surg. Med. *24*, 133–141.

Vargas, G., Chan, K.F., Thomsen, S.L., and Welch, A.J. (2001). Use of osmotically active agents to alter optical properties of tissue: effects on the detected fluorescence signal measured through skin. Lasers Surg. Med. *29*, 213–220.

Velez-Fort, M., Rousseau, C.V., Niedworok, C.J., Wickersham, I.R., Rancz, E.A., Brown, A.P., Strom, M., and Margrie, T.W. (2014). The stimulus selectivity and connectivity of layer six principal cells reveals cortical microcircuits underlying visual processing. Neuron *83*, 1431–1443.

Vinegoni, C., Razansky, D., Figueiredo, J.L., Fexon, L., Pivovarov, M., Nahrendorf, M., Ntziachristos, V., and Weissleder, R. (2009). Born normalization for fluorescence optical projection tomography for whole heart imaging. J. Vis. Exp. *28*, e1389.

Vladimirov, N., Mu, Y., Kawashima, T., Bennett, D.V., Yang, C.T., Looger, L.L., Keller, P.J., Freeman, J., and Ahrens, M.B. (2014). Light-sheet functional imaging in fictively behaving zebrafish. Nat. Methods *11*, 883–884.

Voie, A.H., Burns, D.H., and Spelman, F.A. (1993). Orthogonal-plane fluorescence optical sectioning: three-dimensional imaging of macroscopic biological specimens. J. Microsc. *170*, 229–236.

Vousden, D.A., Epp, J., Okuno, H., Nieman, B.J., van Eede, M., Dazai, J., Ragan, T., Bito, H., Frankland, P.W., Lerch, J.P., et al. (2015). Whole-brain mapping of behaviourally induced neural activation in mice. Brain Struct. Funct *220*, 2043–2057.

Wakamatsu, Y., Pristyazhnyuk, S., Kinoshita, M., Tanaka, M., and Ozato, K. (2001). The see-through medaka: a fish model that is transparent throughout life. Proc. Natl. Acad. Sci. USA *98*, 10046–10050.

Walls, J.R., Coultas, L., Rossant, J., and Henkelman, R.M. (2008). Three-dimensional analysis of vascular development in the mouse embryo. PLoS One *3*, e2853.

Wang, K.H., Majewska, A., Schummers, J., Farley, B., Hu, C.C., Sur, M., and Tonegawa, S. (2006). In vivo two-photon imaging reveals a role of Arc in enhancing orientation specificity in visual cortex. Cell *126*, 389–402.

Weissleder, R. (2001). A clearer vision for *in vivo* imaging. Nat. Biotechnol. *19*, 316–317.

Wen, X., Tuchin, V.V., Luo, Q.M., and Zhu, D. (2009). Controling the scattering of intralipid by using optical clearing agents. Phys. Med. Biol. *54*, 6917–6930.

White, R.M., Sessa, A., Burke, C., Bowman, T., LeBlanc, J., Ceol, C., Bourque, C., Dovey, M., Goessling, W., Burns, C.E., et al. (2008). Transparent adult zebrafish as a tool for in vivo transplantation analysis. Cell Stem Cell *2*, 183–189.

Wickersham, I.R., Finke, S., Conzelmann, K.K., and Callaway, E.M. (2007). Retrograde neuronal tracing with a deletion-mutant rabies virus. Nat. Methods *4*, 47–49.

Wilson, B.C.J., and Steven, L. (1990). Optical reflectance and transmittance of tissues: principles and applications. Quant. Electro. IEEE J. *26*, 2186–2199.

Wong, M.D., Dazai, J., Walls, J.R., Gale, N.W., and Henkelman, R.M. (2013). Design and implementation of a custom built optical projection tomography system. PLoS One *8*, e73491.

Wu, Y.C., Ghitani, A., Christensen, R., Santella, A., Du, Z., Rondeau, G., Bao, Z.R., Colon-Ramos, D., and Shroff, H. (2011). Inverted selective plane illumination microscopy (iSPIM) enables coupled cell identity lineaging and neurodevelopmental imaging in Caenorhabditis elegans. Proc. Natl. Acad. Sci. USA *108*, 17708–17713.

Wu, Y.C., Wawrzusin, P., Senseney, J., Fischer, R.S., Christensen, R., Santella, A., York, A.G., Winter, P.W., Waterman, C.M., Bao, Z.R., et al. (2013). Spatially isotropic four-dimensional imaging with dual-view plane illumination microscopy. Nat. Biotechnol. *31*, 1032–1038.

 ©2016 Elsevier Ltd All rights reserved

Please cite this article as: Susaki and Ueda, Whole-body and Whole-Organ Clearing and Imaging Techniques with Single-Cell Resolution: Toward Organism-Level Systems Biology in Mammals, Cell Chemical Biology (2016), http://dx.doi.org/10.1016/j.chembiol.2015.11.009

Wu, J.P., He, Y., Yang, Z.Q., Guo, C.D., Luo, Q.M., Zhou, W., Chen, S.B., Li, A.A., Xiong, B.Y., Jiang, T., et al. (2014). 3D BrainCV: simultaneous visualization and analysis of cells and capillaries in a whole mouse brain with one-micron voxel resolution. Neuroimage *87*, 199–208.

Yang, H., Wang, H.Y., Shivalila, C.S., Cheng, A.W., Shi, L.Y., and Jaenisch, R. (2013). One-step generation of mice carrying reporter and conditional alleles by CRISPR/Cas-mediated genome engineering. Cell *154*, 1370–1379.

Yang, B., Treweek, J.B., Kulkarni, R.P., Deverman, B.E., Chen, C.K., Lubeck, E., Shah, S., Cai, L., and Gradinaru, V. (2014). Single-cell phenotyping within transparent intact tissue through whole-body clearing. Cell *158*, 945–958.

Yeh, A.T., and Hirshburg, J. (2006). Molecular interactions of exogenous chemical agents with collagen - implications for tissue optical clearing. J. Biomed. Opt. *11*, 014003.

Ying, Q.L., Wray, J., Nichols, J., Batlle-Morera, L., Doble, B., Woodgett, J., Cohen, P., and Smith, A. (2008). The ground state of embryonic stem cell self-renewal. Nature *453*, 519–523.

Yu, T.T., Wen, X., Tuchin, V.V., Luo, Q.M., and Zhu, D. (2011). Quantitative analysis of dehydration in porcine skin for assessing mechanism of optical clearing. J. Biomed. Opt. *16*, 095002.

Yushkevich, P.A., Piven, J., Hazlett, H.C., Smith, R.G., Ho, S., Gee, J.C., and Gerig, G. (2006). User-guided 3D active contour segmentation of anatomical structures: significantly improved efficiency and reliability. Neuroimage *31*, 1116–1128.

Zeng, W., Pirzgalska, R.M., Pereira, M.M., Kubasova, N., Barateiro, A., Seixas, E., Lu, Y.H., Kozlova, A., Voss, H., Martins, G.G., et al. (2015). Sympathetic neuro-adipose connections Mediate leptin-driven lipolysis. Cell *163*, 84–94.

Zhang, B., Li, A., Yang, Z., Wu, J., Luo, Q., and Gong, H. (2011). Modified Golgi-Cox method for micrometer scale sectioning of the whole mouse brain. J. Neurosci. Methods *197*, 1–5.

Zheng, T., Yang, Z.Q., Li, A.A., Lv, X.H., Zhou, Z.Q., Wang, X.J., Qi, X.L., Li, S.W., Luo, Q.M., Gong, H., et al. (2013). Visualization of brain circuits using two-photon fluorescence micro-optical sectioning tomography. Opt. Express *21*, 9839–9850.

Zhu, D., Larin, K.V., Luo, Q.M., and Tuchin, V.V. (2013). Recent progress in tissue optical clearing. Laser Photon. Rev. *7*, 732–757.

Zimmerley, M., McClure, R.A., Choi, B., and Potma, E.O. (2009). Following dimethyl sulfoxide skin optical clearing dynamics with quantitative nonlinear multimodal microscopy. Appl. Opt. *48*, D79–D87.

Zingg, B., Hintiryan, H., Gou, L., Song, M.Y., Bay, M., Bienkowski, M.S., Foster, N.N., Yamashita, S., Bowman, I., Toga, A.W., et al. (2014). Neural networks of the mouse neocortex. Cell *156*, 1096–1111.

Zong, H., Espinosa, S., Su, H.H., Muzumdar, M.D., and Luo, L.Q. (2005). Mosaic analysis with double markers in mice. Cell *121*, 479–492.

Zong, W.J., Zhao, J., Chen, X.Y., Lin, Y., Ren, H.X., Zhang, Y.F., Fan, M., Zhou, Z.A., Cheng, H.P., Sun, Y.J., et al. (2015). Large-field high-resolution two-photon digital scanned light-sheet microscopy. Cell Res. *25*, 254–257.